

Review

Structure Property Relationships and Cationic Doping in $[\text{Ca}_{24}\text{Al}_{28}\text{O}_{64}]^{4+}$ Framework: A Review

John Robert Salasin * and Claudia Rawn *

Materials Science and Engineering, University of Tennessee, Knoxville, TN 37996, USA

* Correspondence: jsalasin@vols.utk.edu (J.R.S.); crawn@utk.edu (C.R.)

Academic Editor: Helmut Cölfen

Received: 20 March 2017; Accepted: 10 May 2017; Published: 16 May 2017

Abstract: $\text{Ca}_{12}\text{Al}_{14}\text{O}_{33}$ (C12A7, $12\text{CaO}\cdot 7\text{Al}_2\text{O}_3$, or $[\text{Ca}_{12}\text{Al}_{14}\text{O}_{32}]^{2+}:\text{O}^{2-}$) is a material with a clathrate cage framework, positively charged and stabilized by anions occluded within 17% of the cages. The occluded anion is modular and can be elemental, polyatomic, and electronic in nature. This review focuses on the electride C12A7 ($[\text{Ca}_{24}\text{Al}_{28}\text{O}_{64}]^{4+}:(4 * \partial)\text{e}^-(2 - \partial)\text{O}^{2-}$), where O_{2-} anions are replaced with electrons, and compliments previous structural and electronic property reviews to illuminate the structure–property relationships. Electride formation is updated with new findings in carbonaceous reduction methods. Most importantly, an extensive compilation of cationic doped C12A7 isostructural compounds is presented as motivation to study doped C12A7 electrides. Cationic dopants have profound impacts on the electronic properties due to changes in the density of states, localized electron behavior, and structural distortions.

Keywords: electride; mayenite; $\text{Ca}_{12}\text{Al}_{14}\text{O}_{33}$; lime-alumina compound; cationic doping; structure–property relationships; $12\text{CaO}\cdot 7\text{Al}_2\text{O}_3$; C12A7

1. Introduction

$\text{Ca}_{12}\text{Al}_{14}\text{O}_{33}$ (C12A7), the mineral mayenite, appears in early cement literature and is the first inorganic electride stable at room temperature. C12A7 crystallizes in the cubic space group $I\bar{4}3d$ (no. 220), with Z (formula units) = 2 and a lattice parameter ~ 12 Å. The unit cell contains 118 atoms and two of the O^{2-} atoms, in the stoichiometric case, nucleate a clathrate cage consisting of tetrahedrally coordinated trivalent Al and octahedrally coordinated divalent Ca cations. The unit cell contains 12 interconnected cages each with a diameter of ~ 5 Å [1–3]. The clathrate cage framework $[\text{Ca}_{24}\text{Al}_{28}\text{O}_{64}]^{4+}$ has a net positive charge balanced by anions occluded in the interior of the cage. In the stoichiometric case, $[\text{Ca}_{24}\text{Al}_{28}\text{O}_{64}]^{4+}:\text{O}^{2-}$, O^{2-} is the template ion responsible for nucleating the framework. The bonding between the framework and the occluded anions leads to a contraction of the cage, introducing structural disorder (Figure 1), which is discussed later.

The C12A7 framework is stabilized with a range of host of oxyanions: O^{2-} [4,5], OH^- [1,6–9], O^- [8,10–14], O_2^- [8,10–16], O_2^{2-} [8,14,16,17] as well as H^- [18–21], F^- [4,8,9,22–24], Cl^- [4,9,22,25], CN^- [9,26,27], S^{2-} [4,9], N^{3-} [9,28], NO_2^- [27], C_2^{2-} [2,29–31], NH_2^- [28,32], hydrazine [27] and Au^- [33]. The interconnectivity of the cages allows high ionic diffusion. Research in the last decade has been heavily focused on the ability for electrons to migrate into the cage framework to satisfy the electrostatic imbalances resulting from anion vacancies, $[\text{Ca}_{24}\text{Al}_{28}\text{O}_{64}]^{4+}:(4 * \partial)\text{e}^-(2 - \partial)\text{O}^{2-}$. As stabilizing anions are removed, electrons migrate into the cages where, when $\partial < 1$, they have a 1s like nature similar to Farbe color centers, leading to the F^+ -like notation used in the literature for metal salts and oxides [34,35]. The ability for these electrons to remain in the cages at room temperature results in $[\text{Ca}_{24}\text{Al}_{28}\text{O}_{64}]^{4+}:(4 * \partial)\text{e}^-(2 - \partial)\text{O}^{2-}$ being the first room temperature inorganic electride.

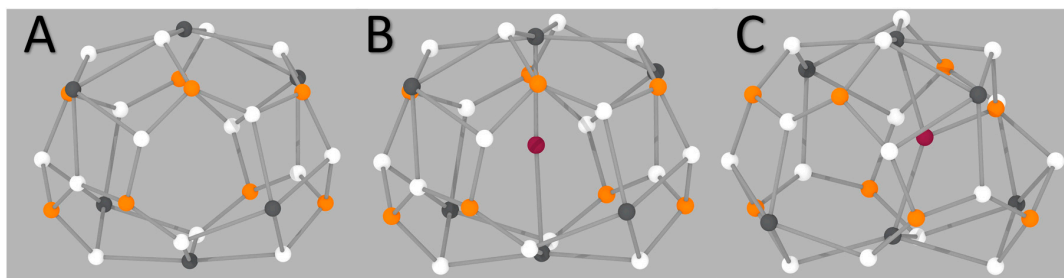


Figure 1. Three main cage types in $[\text{Ca}_{24}\text{Al}_{28}\text{O}_{64}]^{4+}$ framework where Ca atoms are gray, Al atoms are orange, O atoms are white, and the occluded anion is maroon: (A) the unoccupied cage showing no distortion; (B) the $12a$ occupied cage observed in OH^- and e^- occupied cages showing distortion in the axial, S_4 , direction; and (C) the $48e$ off center O^{2-} occupied cage showing a destruction of the framework due to bonding between the framework Ca and Al and the occluded anion.

Dye from Michigan State University has pioneered the synthesis of crystalline organic electrides and defines an electride as “... a stoichiometric ionic crystal in which electrons are trapped in cavities and serve as the counter anions to an equal number of positive charges in a regular crystalline lattice [36].” The electrons are delocalized from their parent atoms and migrate through the positive crystalline frameworks to ensure charge neutrality. This idea of quantum confinement is not new and the reports of localized electrons, e.g., alkali ammonia solutions, ionic solids, and Farbe color centers, predate the 20th century [36]. Dye’s group has successfully synthesized many crystalline organic electrides, where the majority contain cavities 4–6 Å in diameter with 7–9 Å between cage centers [36]. Hosono et al. discovered C12A7 as the first inorganic structure to meet the formal definition of an electride defined by Dye and C12A7 draws similar parallels to the organic structures from the size of the crystalline voids to the observed character of the localized electron [37]. Hosono’s group has since discovered the inorganic electrides including $\text{Ca}_2\text{N}: e^-$ and $\text{Y}_2\text{C}: 2e^-$ and used crystal structure databases and ab initio calculations to find the first magnetic electrides at ambient temperatures [38–40]. The development of stable electrides with a low work function leads to possible applications in electron emission applications, n-doped electronic applications, and catalysis and reduction processes [36,41].

C12A7 research has prompted reviews spanning thermodynamics and synthesis [42], single crystal and thin film growth and the associated electrical properties [2,43], structural disorder and compositional analogs based on the mineral mayenite supergroup [44], and applications in display devices [45]. The goal of this review is to consolidate the structure–physical property relationships, illuminate discrepancies due to the complicated nature of the compound, suggest areas for future research, and investigate the effects of cation doping into the C12A7 clathrate cage framework.

2. Electride Structure–Physical Property Relationships

As the O^{2-} anions are removed in $[\text{Ca}_{24}\text{Al}_{28}\text{O}_{64}]^{4+}:(4 * \partial)e^-(2 - \partial)\text{O}^{2-}$, the cage framework remains with electrons injected into the center of the cage to ensure charge neutrality. The electron is trapped in a potential well created by the positively charged framework, similar to a particle in a box, and exhibits interactions with framework cations [3,34]. When all anions are removed ($\partial = 2$), the theoretical maximum electron concentration is $2.33 \times 10^{21} \text{ cm}^{-3}$ [34]. As ∂ is increased, changes in physical properties are tied to the nature of injected electrons and the resulting structure of the cage framework. This discussion is segmented into three parts; A discussion on insulating stoichiometric C12A7 ($\partial = 0$), semiconducting low and medium electron concentration ($\partial < 1$), and metallic conducting high electron concentration ($\partial > 1$).

2.1. Insulating Stoichiometric ($\partial = 0$)

To fully reveal the atomic structure and the resulting electrical properties as electron concentration increases, neutron and synchrotron x-ray diffraction studies are vital to characterize the underlying

crystallographic changes. An accurate model of the starting stoichiometric structure is needed to fully appreciate the transition to an electrified structure. Several groups, including Palacios et al. and Sakakura et al., started with the stoichiometric system with the intention to move towards the electrified system with varying degrees of electron concentration [46–48]. An in-depth historical synopsis and $[\text{Ca}_{24}\text{Al}_{28}\text{O}_{64}]^{4+} \cdot 2\text{O}^{2-}$ analysis is summarized by Gfellar in his review of mayenite as both a synthetic oxide and mineral [44].

$[\text{Ca}_{24}\text{Al}_{28}\text{O}_{64}]^{4+} \cdot 2\text{O}^{2-}$ is a highly disordered crystal structure. Synchrotron single-crystal x-ray diffraction (SSXRD) conducted by Palacios et al. and Sakakura et al. revealed that the structure of the cage framework ($[\text{Ca}_{24}\text{Al}_{28}\text{O}_{64}]^{4+}$) is a superposition of three cage types; unoccupied, occupied, and adjacent to an occupied cage [46–48]. The disorder arises from the presence of occluded anions needed to nucleate the cage framework. In O^{2-} occupied cages, the occluded anion is located at an off center $48e$ special position and is bonded with two framework Ca and a single framework Al. This leads to contraction of the cage due to bonding between the framework Ca cations and occluded anions. Crystallographically, the contraction moves the Ca cations towards the center from one $24d$ site, Ca1, to two equally partially occupied $24d$ sites denoted Ca1a and Ca1b. Studies by Sakakura et al. suggest that the Ca1a site is moved slightly off the S_4 axis to a $48e$ site. These two sites arise due to the symmetry of the cage and are needed for similar bond lengths between Ca1a/Ca1b and the occluded anion O3 [46,47]. This trimodal split Ca position was previously reported by Nomura et al., however, no split Al position was reported, possibly due to correlating refinement parameters with the site occupancy factor resulting in large uncertainties, especially when the occupation is small [49]. Bonding between Al1-O3 leads to a new Al position, Al1a, causing a destruction of a framework tetrahedron due to a breaking of the framework Al1-O1 bond in favor of the Al1a-O3 bond (Figure 2) [46]. This results in a relaxation of the local structure around this framework tetrahedron and new split positions of both O1 and O2 sites. Further local disorder becomes apparent in adjacent cages where the loss of the attractive force of the Al1 atom results in a distortion of the Ca1 site to $48e$ Ca1c site resulting in the third cage type adjacent to the occupied cages [46]. For a complete listing of crystallographic information, see Table 1 reproduced with modification from Gfellar [44].

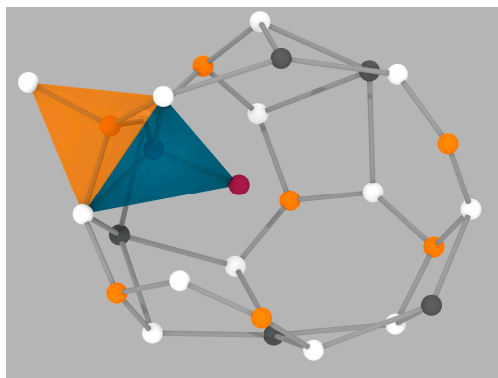


Figure 2. Destruction of framework tetrahedron (orange) due to bonding between occluded O^{2-} , maroon, and framework Al forming a new tetrahedron (blue) in $[\text{Ca}_{24}\text{Al}_{28}\text{O}_{64}]^{4+} \cdot 2\text{O}^{2-}$. The front of the cage has been removed for clarity.

One discrepancy between the two reports of Palacios et al. and Sakakura et al. concerns another occluded anion position on a $12a$ site directly at the center of the cage [46,47]. $[\text{Ca}_{24}\text{Al}_{28}\text{O}_{64}]^{4+} \cdot 2\text{O}^{2-}$ is known to be hygroscopic at ambient humidity [6,22]. In his review Gfellar hypothesized, and both Boysen et al. and Palacios et al. previously hinted, that the presence of the $12a$ occluded site density was due to a hydrolysis reaction between the occluded O and moisture in the atmosphere leading to the reaction $\text{O}^{2-}_{(cage)} + \text{H}_2\text{O}_{(g)} \rightarrow 2\text{OH}^{-}_{(cage)}$ [1,44,47]. Ensuing hydration and diffraction experiments found that stoichiometric samples, when exposed to an atmosphere with a high moisture content, led

to a reduction in occupation of the 48e O3 special position in favor of occupation of the center of the cage 12a site [44]. This 12a site was previously experimentally reported by Boysen et al. in samples with larger than the stoichiometric expected occluded anion occupancy, $[\text{Ca}_{24}\text{Al}_{28}\text{O}_{64}]^{4+} \cdot 2\text{OH}^- \text{O}^{2-}$, and by Nomura et al. [49]. With monovalent occluded species, an increase in occupied cages is expected to be driven by the need to charge balance the positive framework. Upon heating, older reports cite hydroxides (1.3–1.4 wt %) remain in the C12A7 structure up to 1100 °C, however, structural studies by Boysen et al. suggests that at 700 °C the occupation of the 12a site disappears [1,22]. This is consistent with an irreversible loss of the weakly bonded hydroxide. Both the Ca1b and Ca1a sites are present when bonding to O^{2-} but when most other species occupy the cages only the Ca1a site is present due to the location of anions at the 12a, center of the cage, site. Further structural studies of anion substitutions showed that this 12a site is favored by a large number of possible anions that do not have an affinity towards the framework Al, leading to the off center 48e site [50]. The 12a site, along with its hygroscopic nature, further complicates the disorder in the non-stoichiometric $[\text{Ca}_{24}\text{Al}_{28}\text{O}_{64}]^{4+}$ framework leading to an additional cage type, 12a occupied cages. Electron paramagnetic resonance (EPR) has been used for probing the concentration of extra framework paramagnetic species in C12A7 [11,14,37].

Table 1. Comparison of structural models for disordered $\bar{4}3d [\text{Ca}_{24}\text{Al}_{28}\text{O}_{64}]^{4+} \cdot 2\text{O}^{2-}$. Reproduced with modifications from [44]. Occupancies are reported based on the occupancy of the off center and center anion positions to allow for modular structural occupancies based on the degree of OH^- and O^{2-} content.

Name [Occup.]	Wycoff Site		Boysen [1]	Nomura [49]	Palacios [47]	Sakakura [46]
Ca1 [1 – (X + 4Y)]	24d	x	0.1432 (3)	0.1401 (7)	0.13831 (2)	0.13933 (2)
		y	0	0	0	0
		z	0.25	0.25	0.25	0.25
Ca1a [X + 2Y]	24d	x	0.1867	0.1771 (5)	0.17451	-
		y	0	0	0	-
		z	0.25	0.25	0.25	-
Ca1a	48e	x	-	-	-	0.1693 (2)
		y	-	-	-	0.0067 (3)
		z	-	-	-	0.2503 (3)
Ca1b [2Y]	24d	x	-	0.1977 (5)	0.2065	0.2069 (1)
		y	-	0	0	0
		z	-	0.25	0.25	0.25
Ca1c [Y]	48e	x	-	-	-	0.1353 (2)
		y	-	-	-	0.0043 (3)
		z	-	-	-	0.2354 (2)
All [1 – 3Y]	16c	x	0.0188 (1)	0.0189	0.01867 (2)	0.01861 (9)
Alla [Y]	48e	x	-	-	0.30520 (9)	0.3041 (2)
		y	-	-	0.19510 (9)	0.1984 (2)
		z	-	-	0.26090 (9)	0.2619 (2)
Al2 [1]	12b	x	0.875	0.8750	0.875	0.875
		y	0	0	0	0
		z	0.25	0.25	0.25	0.25
O1 [1 – 2Y]	48e	x	0.0367 (1)	0.0381 (1)	0.03612 (4)	0.03605 (4)
		y	0.4429 (1)	0.44290 (8)	0.44231 (4)	0.44234 (3)
		z	0.15054 (9)	0.1510 (1)	0.15049 (4)	0.15052 (3)
O1a [Y]	48e	x	-	-	-	0.1302 (3)
		y	-	-	-	0.0603 (3)
		z	-	-	-	0.4328 (3)
O1b [Y]	48e	x	-	-	-	0.1718 (5)
		y	-	-	-	0.0312 (4)
		z	-	-	-	0.4352 (5)
O2 [1 – 3Y]	16c	x	0.18519 (9)	0.1865 (1)	0.18526 (3)	0.18510 (4)
O2a [Y]	48e	x	-	-	-	0.1996 (6)
		y	-	-	-	0.1750 (7)
		z	-	-	-	0.1893 (6)
O3 (center) [X]	12a	x	0.375	0.375	0.375	-
		y	0	0	0	-
		z	0.25	0.25	0.25	-
O3 (off cen.) [Y]	48e	x	-	0.344 (2)	0.3588 (2)	0.3559 (6)
		y	-	0.036 (2)	0.0616 (2)	0.0614 (7)
		z	-	0.243 (5)	0.2479 (2)	0.2506 (7)

The structural disorder in the stoichiometric case results in a complicated band structure calculated through density functional theory (DFT). Theoretical calculations of the band structure corresponding to $[\text{Ca}_{24}\text{Al}_{28}\text{O}_{64}]^{4+}:(4 * \partial)\text{e}^{-}(2 - \partial)\text{O}^{2-}$ with various levels of ∂ have proven difficult due to the conversion of the system from an insulating to a metallic state, however, similar trends are observed from a variety of different functionals [3,34,51,52]. Sushko et al. performed band structure calculations from the stoichiometric insulating state to the electrified state using two different density functionals; B3LYP works well with insulating systems and LDA works well with metallic systems [3]. $[\text{Ca}_{24}\text{Al}_{28}\text{O}_{64}]^{4+}:\text{2O}^{2-}$ has a large bandgap, $E_g = 6\text{--}7\text{ eV}$, making it electrically insulating [51]. Many interstitial electronic states reside in the band gap (Figure 3A), and form two general groups, 1–2 eV above the valence band (VB) and 0.5–2 eV below the conduction band. The grouping of ten states below the conduction band corresponds to the ten unoccupied cages, deemed the cage conduction band (CCB). The presence of this conduction band makes C12A7 a system where two conduction bands are observed; the states associated with framework cations and those corresponding to the cage potential well. The states above the valence band correspond to two different features. The eight states between -4.0 and -5.0 eV correspond to O 2p states split off from the valence band due to disorder associated with the bonding between framework Al and occluded O^{2-} ; this is due to the presence of oxygen splits positions in the $48e$ occupied cage type. The two states above -4.0 eV correspond to O^{2-} occupied CCB states [3]. The contraction of the cage due to interactions with occluded species move occupied CCB states to lower energies. Other band structure calculations only exhibit the two occupied CCB states near the valence band. Sushko et al. reported that if the off-center O^{2-} position was discarded in favor of a metastable center of the cage position, historically reported in diffraction studies, the 2p states associated with the framework did not split from the valence band and only two bands, corresponding to the two O^{2-} occupied cages, are observed [3]. This is understandable, without the off-center O^{2-} position there will be higher homogeneity in the O's contained in the framework. These 12 states of the CCB account for all 12, unoccupied and occupied, cages in the unit cell of C12A7, and the structure of the cage correlates to the energy of these states giving rise to the interesting electrical properties.

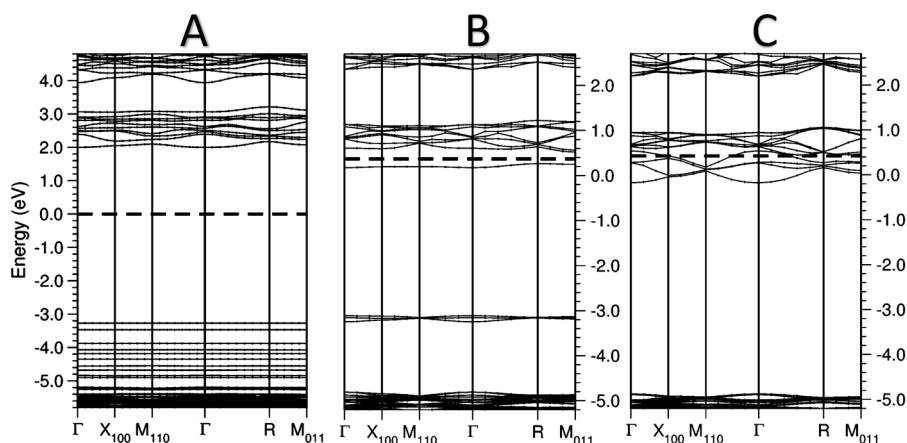


Figure 3. Band structure of: (A) $[\text{Ca}_{24}\text{Al}_{28}\text{O}_{64}]^{4+}:\text{2O}^{2-}$; (B) partially reduced $[\text{Ca}_{24}\text{Al}_{28}\text{O}_{64}]^{4+}:(\alpha)\text{e}^{-}(4 - \alpha)\text{H}^{-}$; and (C) fully reduced $[\text{Ca}_{24}\text{Al}_{28}\text{O}_{64}]^{4+}:\text{4e}^{-}$ calculated using B3LYP and LDA functionals. “ $3 \times 3 \times 3$ k mesh was used in both cases, the Fermi level is shown as a thick dash line, and only spin up states are shown.” Adapted with permission from [3]. Copyright 2007 American Chemical Society.

Due to the large band gap, C12A7 single crystals exhibit >90% optical transparency in the visible range, and at low electron concentration C12A7 combines optical transparency with electrical conductivity leading to potential applications as a transparent conductive oxide that is both inexpensive and earth abundant [52–54].

2.2. Semiconducting Low/Medium Electron Concentration ($\partial < 1, n_e < 1 \times 10^{21}$)

At low and medium electron concentration, C12A7 transfers into a semiconducting state. The introduction of electrons into the cages results in a color change from clear to green, which is characteristic of F^+ centers.

The structure is now more disordered with a new electron occupied cage type in addition to the previous cage types. Palacios et al. performed SSXRD looking at low electron loadings and determined that, as electron loading increased from $[Ca_{24}Al_{28}O_{64}]^{4+}:0.6e^-1.7O^{2-}$ to $[Ca_{24}Al_{28}O_{64}]^{4+}:1.8e^-1.1O^{2-}$, the lattice parameter increased by 0.05% and 0.21%, respectively [47,48]. This is consistent with the relaxation of the occupied cage type toward an unoccupied cage type due to weakened interaction between the localized electron and the framework. A decrease in both the Ca1a and Ca1b site occupancies with increased electron loading further substantiates this theory. It was reported that there was a small increase in the Ca1a-Ca1b (occupied cage diameter) while Ca1-Ca1 (unoccupied cage diameter) did not change [47]. The occupied cage diameter is contracted with respect to the unoccupied cage diameter due to the bonding between framework Ca and the O^{2-} . As the occupancy of O^{2-} is reduced, there should be no change in the bonding behavior leading to a relaxation in Ca1a/Ca1b positions. The observed change in contracted cage diameter could be attributed to the averaging of all the cage types. There are two likely possibilities; As the O3 and Ca1a/Ca1b occupancy decreases and the Ca1 occupancy increases, the refinement may be compromised due to difficulties distinguishing between the heavily correlated Ca1 and split positions, leading to inaccuracy in the atomic coordinates, and the second being a weak interaction between the localized electron and the framework Ca leading to a split Ca position in between Ca1 and Ca1a/Ca1b. As the electron occupied cage type increases in relevance the averaging of the split Ca position, corresponding to e^- occupied cages and Ca1a/Ca1b would lead to a larger contracted cage diameter. This evidence points to a contraction of the cage due to interaction with occluded electrons. Palacios et al. found that electron scattering density, at the 12a center of the cage position in reduced compositions, increased as electron loading increased [47]. This, experimentally, suggests that the electron is localized in the cage and the localized electron is located at the 12a center of the cage position as predicted by theoretical models [34,55]. However, since it is likely that the stoichiometric samples Palacios et al. studied were exposed to moisture, it is possible, since electron doping has not reached a maximum, that moisture caused the formation of hydroxide species leading to the observed electron density on the 12a position in reduced samples. The experimental observations from SSXRD are corroborated by band structure calculations.

Band structure calculations corresponding to low e^- occupation results in occupied CCB states 0.4–1 eV below the CCB and the small dispersion of this state indicates high localization of the electron [3]. It should be noted that these band structures were calculated through modeling of $[Ca_{24}Al_{28}O_{64}]^{4+}:(\alpha)e^-(4-\alpha)H^-$ and not $[Ca_{24}Al_{28}O_{64}]^{4+}:(4*\partial)e^-(2-\partial)O^{2-}$. This allows for calculations to be performed at lower electron concentration and both B3LYP and LDA functionals give similar band structures for the low electron loaded models. The calculated occupied cage diameter associated with the localized electron increases from 4.39 Å in O^{2-} occupied cages to 5.07 Å, which is, however, still significantly less than the unoccupied cage diameter of 5.6 Å. The average of these two cage diameters corroborates the diffraction observations associated with the expansion in average occupied cage diameter suggesting that localized electrons are polarons and induce cage framework contractions. This reduction in contracted cage diameter raises the energy of e^- occupied CCB states towards the unoccupied CCB, and the gap between the occupied and unoccupied CCB states gives rise to a semiconducting state [3].

The optical absorption spectra displays two peaks centered near 2.8 and 0.4 eV [29,56]. The absorption of these two peaks are assigned to the 1s to 2p excitation of a localized electron in a single cage, consistent with F^+ color centers, and to the transition of localized electrons between cages, respectively [2,21,56]. Optical reflectance data show sharp phonon lines in the infrared regime as well as absorption in the visible and ultraviolet range typical of insulators. Limited Drude response is observed and contributions to the reflectance pattern can be fit with a Lorentzian model further indicating

the dominate carrier type is localized opposed to free carriers [51,52]. Temperature dependent DC conductivity measurements when $\partial < 0.5$ reveal a temperature dependence of $\log(\sigma)$ of T^{-1} suggesting that at low concentrations the electrons conduct as polarons [37]. This indicates a strong lattice-electron coupling as previously observed in diffraction experiments and in DFT calculations and the activation energy (0.1 eV) and mobility ($0.1 \text{ cm}^2 \cdot (\text{Vs})^{-1}$) are consistent with polaron theory [37,51,57]. As ∂ increases to 1, electrons form bipolarons due to neighboring cages being occupied, limiting polaron type conduction, and a change in the temperature dependence to $T^{-1/4}$ is consistent with thermally activated variable range hopping (VRH) conduction [2,37,51,58]. In the semiconducting state a room temperature electrical conductivity (σ_{RT}) below $100 \text{ S} \cdot \text{cm}^{-1}$ is obtained [2].

The presence of bipolarons is confirmed through analysis of EPR trends. Localized electrons act as F^+ -like centers in a paramagnetic spin state [43]. This paramagnetic nature allows for the concentration of localized electrons to be determined by EPR. However, it was observed by Matsuishi et al. and corroborated by Kim et al. that the EPR signal saturates at approximately 8×10^{19} electrons [37,59]. This is only 1% of the theoretical maximum electron concentration and further statistical analysis determined that at peak electron loading there is a 99% chance of a neighboring cages being occupied. This suggests that, as electron concentration increases, neighboring electrons alter the paramagnetic state of the localized electron. Matsuishi et al. [37], further confirmed by Kim et al. [2], proposed that these neighboring electrons would form an EPR invisible bipolaron. Due to this fact, EPR should not be used to determine electron concentration unless ∂ is small, but can be used to identify the presence of F^+ paramagnetic centers characteristic of localized electrons at all levels of electron concentration.

2.3. Metallic High Electron Concentration ($\partial > 1, n_e > 1 \times 10^{21}$)

In the semiconducting state electrons are localized in the cages due to electron framework interactions leading to a large degree of inhomogeneity of cage types. As electron concentration increases past 1×10^{21} samples demonstrate a loss of optical transparency and a color change to black corresponding to absorption in the full visible range. DC conductivity measurements show a negative trend of $\log(\sigma)$ with respect to temperature, and metallic like conduction of approximately $1500 \text{ S} \cdot \text{cm}^{-1}$ with an increase in carrier mobility to $4.0 \text{ cm}^2 \cdot (\text{Vs})^{-1}$ is observed [58].

As electron concentration is increased, the degree of disorder associated with O^{2-} occupied cages is reduced due to the limited concentration of stabilizing anions. Kim et al. conducted synchrotron powder XRD (SPXRD) on $[\text{Ca}_{24}\text{Al}_{28}\text{O}_{64}]^{4+} : 4e^-$ and analyzed the data combining maximum entropy method (MEM) and Rietveld refinement techniques. No split positions were reported for $[\text{Ca}_{24}\text{Al}_{28}\text{O}_{64}]^{4+} : 4e^-$ and no electron scattering density was observed at the center of the cage, in contrast to reports in the semiconducting state by Palacios et al., suggesting a full relaxation of the contraction associated with electron occupied cages and loss of localized electrons which leads to a homogeneity among cage types [57].

Band structure calculations when $\partial = 2$, maximum electron concentration, show four occupied CCB states corresponding to the e^- occupied cages as well eight states corresponding to the unoccupied cages. B3LYP predicted a semiconducting system while LDA, displays no observable bandgap between the occupied CCB and unoccupied CCB [3]. A closer look reveals that one of the occupied CCB states is at a higher energy than the unoccupied CCB creating a metallic system matching the observed DC conductivity results. Further, a higher dispersion of these states suggests that an increase in carrier density leads to the formation of delocalized free carriers [3,57]. The calculated cage diameter of electron occupied cages has increased to $\sim 5.4 \text{ \AA}$, which is only slightly ($\sim 0.2 \text{ \AA}$) smaller than the unoccupied cage diameter and explains why no split positions were observed in powder diffraction experiments.

Seebeck coefficient measurements reveal a decrease in Seebeck coefficient with increased carrier concentration and a change in sign concurrent with the transition from a semiconducting to a metallic state. This provides insight into the density of states (DOS) around the Fermi energy as electron concentration is increased indicating valleys in the DOS, confirmed through band structure calculations

(Figure 4 (left)). The DOS around the lower CCB corresponds to Ca s-projected contribution and the higher CCB states have a Ca d-projected contribution [60]. With increased electron concentration, the occluded electrons that are initially localized in a s-like F^+ state change to the sd-hybridized state of Ca (Figure 4 (right)). This hybridized state plays a role in the observed superconducting transition at ~ 0.2 K due to the increased ability for Cooper pairs to form [58,60].

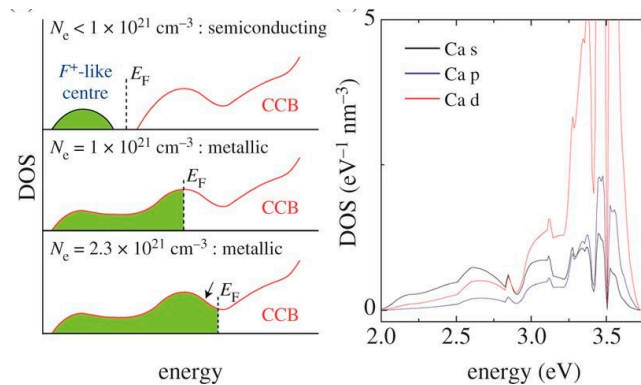


Figure 4. (left) Schematic illustration of DOS around the Fermi level as unoccupied and occupied CCB merge with increasing electron concentration. (right) Partial DOS of the CCB corresponding to the Ca s, d, and p DOS. Modified from Hosono et al. [60].

Optical reflectance studies find that as electron concentration is increased a Drude peak and broadening of phonon peaks in the IR region, characteristic of free electron carriers, is observed in conjunction with the characteristic Lorentzian transitions associated with localized carriers [51,52]. The dominant conductivity type changes from VRH conduction to band conduction, but the Lorentzian features suggests both forms of conduction occur concurrently [51,52]. Lobo et al. identified an increase in asymmetry of phonon peaks with increased carrier concentration in the metallic regime. This is characteristic of the Fano effect and indicates a large lattice–electron coupling. The observance of an increased Fano effect with carrier concentration confirms that localized and delocalized carriers are observed in the metallic state and the increase in carrier concentration favors the formation of polarons. There have only been EPR studies conducted just up to the metal transition, and paramagnetic electron species are still observed [37]. These experimental results along with the theoretical calculations point to the presence of localized and delocalized electrons existing in the C12A7 leading to concurrent and cooperative types of electrical conduction [43,52].

2.4. Summary

C12A7 exhibits an insulator to metal transition heavily correlated to structural changes. As anions are removed, and electrons are injected into the structure, the initial insulating disordered system relaxes to a less disordered metallic system due to a loss of off centered O^{2-} occupied cages. A weaker interaction between localized electrons, occupying the center of the cage, and framework Ca leads to a relaxation of the occupied cage diameter toward the unoccupied cage diameter resulting in an increase in homogeneity of the cages. This relaxation of the system is observed in theoretical band structure calculations and results in the occupied CCB states rising in energy until they overlap with the unoccupied CCB states leading to delocalization of electrons over all cages and metallic conduction. Electrical conductivity and optical reflectance measurements support the insulator to semiconductor to metallic conductor transition observed in band structure calculations. However, since the occupied cages do not fully relax back to the unoccupied state there is still some degree of electron localization. Structural, experimental, and theoretical studies conclusively point to the same trends in C12A7.

The diffraction studies by Kim et al. raise some important questions on the contraction of electron occupied cages. Does SPXRD have enough resolution to deconvolute the heavily correlated split

positions and reveal small scattering due to localized electrons in the cage? There are inconsistencies between diffraction studies and possibly disagreement between diffraction studies and theoretical calculations in the metallic regime. Due to the hygroscopic nature of stoichiometric C12A7 it is important that all samples are handled consistently to avoid contamination. A systematic study across all electron concentrations, from insulating to metallic, with careful contamination control is needed to compliment physical property studies by Lobo et al. and Matsuishi et al. Neutron diffraction studies probe the nuclear density, making it invisible to the localized electrons, while synchrotron diffraction studies probe the localized electrons and induced electrostatic distortions in electron clouds. Combined, they paint two different pictures of the same system and single crystal diffraction experiments at high electron concentration are needed.

Convoluting cooperative electronic conduction, observed at peak electron loading, is complicated. However, the current theory for the conversion from localized carrier to free carriers does not explain the increase in phonon electronic coupling observed through the Fano effect. While it may be related to the sd-hybridization proposed by Hosono et al. research to understand the behavior of polarons and free carrier conduction at peak electron loading can illuminate the mechanism behind the Fano effect observed by Lobo et al.

3. Electride Formation Processes

3.1. C12A7 Synthesis

C12A7 melts congruently and single crystals can be grown through many techniques including float zone (FZ), Czochralski (CZ), and melt forming techniques [2,47,56,61,62]. C12A7 is an intermediate compound in the CaO and Al₂O₃ binary system sandwiched between the two-phase regions consisting of C12A7 and either secondary phases denoted CA (CaAl₂O₃) and C3A (Ca₃Al₂O₆) (Figure 5). These two secondary phases are the formation products of C12A7 at higher temperatures (≥ 1200 °C), normally through solid-state synthesis, and decomposition products when no anions are present to stabilize the cage framework at high temperatures [63,64].

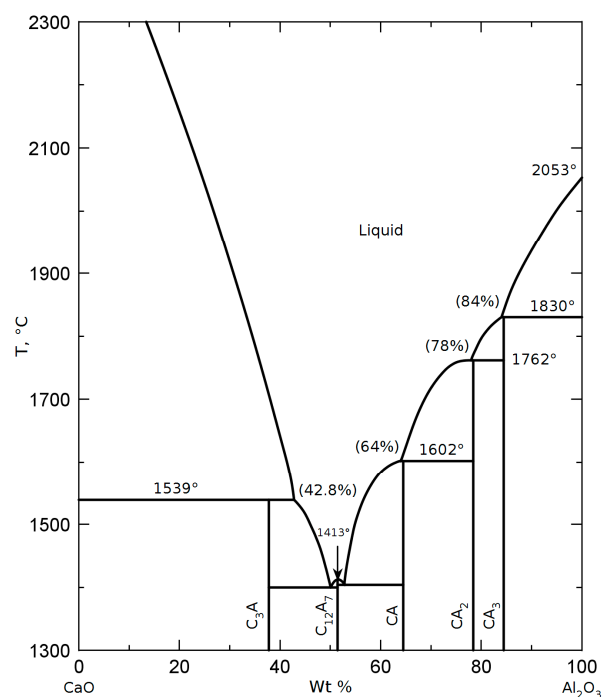


Figure 5. Binary CaO-Al₂O₃ phase diagram with Ca₁₂Al₁₄O₃₃ at ~54 wt % Al₂O₃ [65].

Wet chemistry processes can be used to synthesize C12A7 below 900 °C. It is suspected that the formation reaction proceeds through a secondary phase which is metastable, C5A3 ($\text{Ca}_5\text{Al}_6\text{O}_{14}$) [63,64,66]. There is a small stoichiometric difference between the C12A7 and C5A3, $9 \text{Ca}_5\text{Al}_6\text{O}_{14} + \text{Ca}_3\text{Al}_2\text{O}_6 \rightarrow 2 [\text{Ca}_{24}\text{Al}_{28}\text{O}_{64}]^{4+} : 2\text{O}^{2-}$. C5A3 consists of layered octahedrally coordinated Ca and tetrahedrally coordinated Al cations similar to the C12A7 cage framework (Figure 6). When the extra oxygen is available, it nucleates the clathrate cage framework. C5A3 and C3A are decomposition products, observed by Palacios et al. and our own investigations (discussed below), at 1100 °C under dry vacuum conditions [4,48].

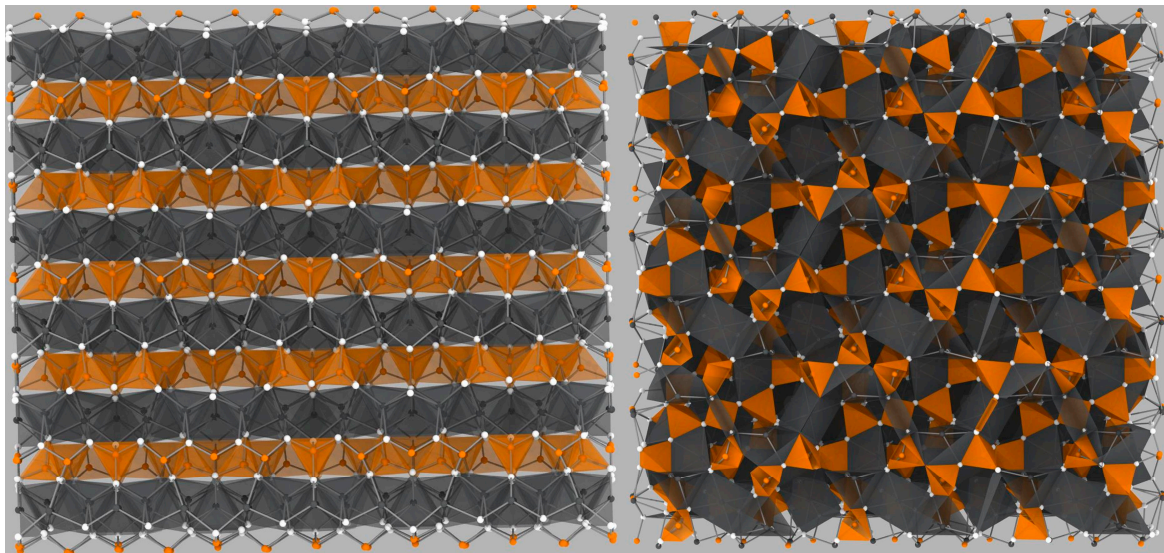


Figure 6. Comparison of layer C5A3 structure on the left and the C12A7 cage structure on the right.

Exploiting the affinity of weakly bonded occluded anions to form more stable bonds and high ionic diffusion afforded by the clathrate cage framework is the foundation of currently developed $[\text{Ca}_{24}\text{Al}_{28}\text{O}_{64}]^{4+} : (4 * \partial)\text{e}^- (2 - \partial)\text{O}^{2-}$ electride formation processes. The electride formation processes can be divided into two groups with varied processing parameters: processes that extract the occluded anion species and those replacing occluded species.

3.2. Extraction Formation Processes

The occluded O^{2-} anions exhibit a high affinity to form more stable bonds, the basis of many reduction processes, and C12A7 electride formation extraction processes focus on using bulk metals and C as reducing agents.

3.2.1. Metal Reduction Processes

Metal extraction methods involve reacting the occluded O^{2-} anions with metals to form metal oxides. Ca metal is unstable and readily reacts with O_2 and H_2O in ambient atmosphere to form H_2 gas. Matsuishi et al. exploits this instability to form electride float-zone (FZ) single crystals, sealed in an evacuated (10^{-4} Pa) quartz ampule with Ca metal shot at a reduction temperature of 700 °C [37]. As process duration is increased, the initially clear single-crystals demonstrate the characteristic color change through green to black. After 240 h the carrier density (n_e) and electrical conductivity at room temperature (σ_{RT}) saturate at 2×10^{21} , which is close to the theoretical 2.33×10^{21} if all occluded O^{2-} is removed, and $100 \text{ S}\cdot\text{cm}^{-1}$, respectively [37,47]. O^{2-} diffuses to the surface where it reacts with Ca in the vapor phase, $\text{O}_{(cage)}^{2-} + \text{Ca}_{(g)} \rightarrow \text{CaO}_{(surface)} + 2\text{e}_{(cage)}^-$. After the process, the samples are encased in CaO layer that has to be mechanically removed. This layer has negative processing impacts as it limits the processing temperature to 700 °C due to the increase in Ca stoichiometry, derived from the

CaO layer, which moves the phase equilibria into a two phase C12A7 and C3A region. Further this CaO layer limits the application of this process to thin high surface area samples due to the oxygen inability to diffuse through this CaO layer to react with metallic Ca, thereby turning off the electride formation process.

Matsuishi et al. exploit the formation of the CaO phase by starting the system off equilibrium to use the CaO to directly synthesize $[\text{Ca}_{24}\text{Al}_{28}\text{O}_{64}]^{4+} : 4e^-$ powder [67]. The process involves reacting a C12A7 and CA mixture with Ca shot at 700 °C for 15 h in an evacuated (10^{-4}) sealed quartz tube. Subsequent grinding, resealing, and firing at 1100 °C for 2 h led to the formation of the black C12A7 electride powder. This process was also carried out utilizing CaH_2 at 600–700 °C for 15 h, and found that dehydration of OH^- occupied cages to O^{2-} before reduction increased electron concentration suggesting that OH^- cannot be extracted by Ca oxidation [68]. Understanding that anions are needed to nucleate the clathrate framework, in this study, where there are no obvious template anions, suggests that direct C12A7 electride can be accomplished when the electride phase already exists. This same idea was observed when FZ single crystals were grown from a polycrystalline C12A7 feed rod and single crystal electride seed. When the electride seed was attached to a non-electride feed rod, it resulted in the formation of the electride phase [2,69]. Future experiments should explore different bulk metals in a hope of directly synthesizing doped C12A7 electrides and further investigate direct electride formation processes.

Kim et al. improved the Ca metal shot process by changing the reactive metal shot to Ti powder [2,57]. The resulting metal oxide film has the composition $\text{Ti}_x\text{O}_{2-x}$, where $1 \leq x \leq 2$, a non-stoichiometric oxide [70]. This allows for continual oxygen diffusion through the metal oxide layer allowing the process to be employed for single crystals of any size. The Ti extraction method also allows for the processing temperature to be raised up to 1300 °C due to the stability of the C12A7-Ti $_x\text{O}_{2-x}$ system [71]. This increase in processing temperature leads to an increase in O^{2-} diffusion in C12A7 resulting in shorter processing times [2]. Czochralski (CZ) grown single crystals ($5 \times 5 \times 15 \text{ mm}^3$) were fired at 1100 °C in an evacuated (10^{-1} Pa) sealed quartz tube, and reached a n_e of 2.3×10^{21} and σ_{RT} of $1500 \text{ S}\cdot\text{cm}^{-1}$ after a reduction process time of 24 h compared to 240 h in the Ca method [57]. The increase in σ_{RT} is contributed to an increase in n_e and carrier mobility (μ_e) associated with metallic band conduction [2]. Ali et al. found that ideal reduction time and temperature was 48–60 h at 1100 °C and an increase in temperature to 1200 °C led to a decomposition of the C12A7 phase and an increase in duration led to a brittle sample and a large reduction in conductivity [72].

Palacios et al. applied a similar process with a different form of Ti and single crystal geometry [47]. Melt formed crystals are wrapped in a Ti foil and sealed in an evacuated (10^{-2} Pa) quartz tube and fired at 1000 °C. After a processing time of 48 h, the specimen showed a color change from clear to green and n_e was estimated, through analysis of SSXRD data, refining on the occluded anion site occupancy factor (sof), to be approximately 1.0×10^{21} . An increase in processing time to 144 h yielded black samples with a n_e of approximately 2.3×10^{21} [47]. The increase in process duration could be due to a smaller surface area associated with the Ti foil leading to less vapor transport as well as a decrease in temperature leading to a decrease in O^{2-} diffusion. The foil process needs further investigation as there was no mention of having to mechanically remove a TiO_2 layer in the reports by Palacios et al., and the size and irregular geometry of the melt formed crystals would make mechanical removal of this oxide layer difficult. Palacios et al. [48] also report using V foil and even a V sample container for neutron powder diffraction (NPD) experiments to reduce powder and melt formed single crystal samples. In the V foil process powder samples are fired at 1000 °C surrounded by the V foil in an evacuated (1.3×10^2 Pa) sealed quartz tube and in the V container process powder samples are sealed in an evacuated (10^{-3}) V-can and fired at 1100 °C for 8 h. In the V-can reduction process, electride formation was observed in the temperature range of 700 to 1100 °C, however, during the 8 h dwell at 1100 °C C12A7 decomposed to C5A3 and C3A.

Metal extraction techniques are ideal on single crystals where high process temperatures and times and post processing techniques are not an issue. Stable metal foil extraction methods show

promise for processing of polycrystalline samples, and if metal oxides are formed in the process a direct synthesis route to doped $[\text{Ca}_{24}\text{Al}_{28}\text{O}_{64}]^{4+}:(4 * \delta)e^{-}(2 - \delta)\text{O}^{2-}$ may be easily realized.

The metal extraction technique cannot be applied to thin films; however, Miyakawa et al. developed a technique, similar in principle to the metal reduction method, utilizing an oxygen deficient C12A7 layer to reduce the previously deposited thin film below [73]. The oxygen deficient C12A7 replaces the metal as the reducing agent with a high affinity toward oxygen. C12A7 thin films were grown using pulsed laser deposition (PLD) where an amorphous C12A7 was deposited at room temperature and then crystallized in air at 1100 °C. The thin film was placed back into the PLD system where another amorphous C12A7 layer was deposited under vacuum conditions at 700 °C. This top layer would be oxygen deficient and act as a reduction agent for the polycrystalline C12A7 thin film previously deposited. After mechanical removal of the top layer the resultant thin film displayed electrical conductivity as high as $800 \text{ S}\cdot\text{cm}^{-1}$. This process has been repeated on $\text{Sr}_{12}\text{Al}_{14}\text{O}_{33}$ (S12A7) thin films and S12A7/C12A7 layered thin films, which is discussed later [74].

3.2.2. Carbonaceous Atmosphere Process

The second extraction method, CO/CO₂ reducing atmosphere, is fundamentally different than the previous reactive metal shot techniques. Kim et al. developed the process which can be performed on any starting form, including polycrystalline powder, thin films, or single crystals [2,59]. The advantage over the metal shot technique is the reduction reaction occurs in the gas phase, allowing for sample surfaces to remain unaffected during the process. Samples are placed in a graphite crucible, with a lid, under flowing inert gas. It is suspected that inside the crucible a strong carbon monoxide reducing atmosphere is formed reacting with the occluded O^{2-} to form CO/CO₂ gas, $\text{O}_{(\text{cage})}^{2-} + \text{CO}_{(\text{g})} \rightarrow \text{CO}_{2(\text{g})} + 2e_{(\text{cage})}^{-}$. A FZ single crystal sample fired at 1200 °C for 0.5 h produced a σ_{RT} of $4 \text{ S}\cdot\text{cm}^{-1}$. EPR was used to determine carrier concentration, which can only identify carriers in the paramagnetic state. Therefore, actual carrier density is unable to be confirmed, and higher degrees of reduction may result by increased process times and/or temperatures. If this proposed reduction reaction occurs, the graphite crucible can be removed and the entire process can be conducted with flowing CO gas allowing for quick batch processing. This is confirmed by electrical conductivity measurements on Fe-doped C12A7 FZ single crystals where electrical conductivity increased after processing in a CO/CO₂ atmosphere at 800, 900, and 1000 °C [75].

The CO/CO₂ reduction technique is versatile and can be applied to all sample types and geometries leading to electron loading at moderate process temperatures. However, the degree of maximum electron concentration needs to be investigated and long process durations may be needed to achieve a high degree of electron loading.

3.3. Replacement Formation Processes

Replacement reduction techniques work by replacing the occluded species and subsequently altering the replacement anion for localized electron generation. Currently, two main processes replacing the stoichiometric occluded anion O^{2-} have been developed with H^{-} and C_2^{2-} .

3.3.1. H^{-} Replacement and Photoionization Process

A H₂ gas reduction process allows for low levels of electron loading due to replacement of O^{2-} and subsequent ionization of hydrogenous species. Hayashi et al. first published the light-induced insulator to conductor conversion of C12A7 [21]. FZ single crystal samples underwent a firing process at 1300 °C in a flowing H₂ reducing atmosphere consisting of 20% H₂ and 80% N₂. After the samples were processed at 1300 °C for 2 h the single crystals were quenched to room temperature where no color change was observed and the σ_{RT} was low (insulating). Spectroscopy analysis showed the single crystals had a large concentration of H^{-} anions confirming that the anion replacement process had succeeded through the following chemical reaction, $\text{O}_{(\text{cage})}^{2-} + \text{H}_{2(\text{g})} \rightarrow \text{OH}^{-}_{(\text{cage})} + \text{H}^{-}_{(\text{cage})}$ [21].

Theoretical calculations by Sushko et al. suggest that the H₂ gas decomposes to an H⁺ and H⁻ pair in the C12A7 framework [76]. The H⁻ anion is localized in the center of the cage stabilizing the clathrate framework. The H⁺ ion diffuses through the sample until it bonds to an occluded O²⁻ anion, creating an occluded OH⁻ anion, or until it bonds to an oxygen in the clathrate framework [76]. After subsequent processing via UV light irradiation, with a flux of approximately 10²⁰ photons·cm⁻², the sample demonstrated the characteristic green color change associated with localized electrons and a σ_{RT} of 0.3 S·cm⁻¹ [21]. The UV irradiation forms C12A7 electride by ionizing the H⁻ ion forming elemental H and an electron, $H_{(cage)}^- \rightarrow H^0_{(cage)} + e^-_{(cage)}$. Theoretical calculations find that the elemental H is unstable and will thermally release another electron ionizing to an H⁺ anion. This anion then diffuses through the system until it bonds with framework or occluded O anions as previously discussed. This leads to the following reaction after the complete ionization process: $H_{(cage)}^- + O_{(cage)}^{2-} + null_{(cage)} \xrightarrow{UV, \lambda} OH_{(cage)}^- + 2e^-_{(cage)}$ [76,77]. This ionization is stable after irradiation has stopped, however at 320 °C the oxygen bonded protons and electrons recombine to form a H₂ molecule in a cage and the characteristic properties of the localized electrons are lost. Upon further heating to 550 °C H₂ gas is released from the sample and subsequent UV irradiation results in no formation of localized electrons [21].

Bertoni et al. conducted a similar process on polycrystalline samples where after processing sintered pellets, in a 4% H₂/96% N₂ forming gas at 1300 °C for 2 h, subsequent irradiation, using a Hg lamp (275–650 nm) for approximately 1 h, yielded electride C12A7 with a conductivity on the same order of magnitude as the single crystal [78]. These polycrystalline samples showed a decrease in decomposition temperature from 300 to 135 °C, the origin of which is unclear. The H₂ gas reduction process results in a lower electrical conductivity and carrier concentration associated with limited replacement between the O²⁻ occluded anions with H⁻ anions.

Sushko et al. [76] proposes treating [Ca₂₄Al₂₈O₆₄]⁴⁺:4e⁻, formed through another reduction process, to obtain the fully H⁻ replaced compound. Hayashi builds on this idea by employing a CaH₂ reduction process to obtain the highest concentration of [Ca₂₄Al₂₈O₆₄]⁴⁺:4H⁻ [20]. Stoichiometric FZ grown single crystals and electride single crystals were processed at 800 °C for various process times in sealed and evacuated quartz ampules and these samples were compared to FZ single crystals fired at 1300 °C for 6 h at 0.2 atm H₂. He found that reproducibility was poor and process duration had no clear dependence on H⁻ inclusion. Improvement was found when the CaH₂ and samples were wrapped in Pt foil due to increased contact area between the reduction agent and the samples as well as the reduction of O species diffusion through or supplied by the silica tube. The samples were then ground to remove a containment layer on the outside of the single crystals. After 240 h, the H⁻ concentration was estimated to be ~2 × 10²¹, corresponding to the highest replacement [Ca₂₄Al₂₈O₆₄]⁴⁺:4H⁻ and the lattice parameter was determined to be approximately 11.97 Å, smaller than stoichiometric C12A7 and similar to other fully monovalent balance C12A7 [77]. It was found that after ionization, samples with only half of the theoretical maximum H⁻ produced the highest electron concentrations and electron concentration decreased with decreasing O²⁻ content [77]. This verifies the ionization mechanisms and determines that the increasing H⁻ towards the maximum does not increase electron generation. "...the theoretical maximum number of photo generated electrons per unit cell is determined by the smaller value of either 2[H⁻] or 2[O²⁻] [77]". This process is similar to that conducted in the synthesis of powder electride C12A7 by Inoue et al., however, in their results no evidence due to H⁻ was observed in the absorption spectrum [68]. One explanation could be tied to the short processing time in comparison to the process conducted by Hayashi.

3.3.2. Carbide Replacement Process

The second replacement reduction technique involves the replacement of O²⁻ with C₂²⁻ that is suggested as a high temperature anion with the ability to stabilize the clathrate framework. The carbide anion has the same valence and similar ionic radii as O²⁻, 1.2 Å and 1.4 Å, respectively [29]. It is believed that the carbide ion stabilizes the crystallization of the clathrate framework at high

temperatures and then decomposes to 2C or 2CO on cooling [29]. This replacement reaction was first found by Kim et al. while trying to directly synthesize reduced C12A7 single crystals from a high temperature melt under a reducing atmosphere [29]. C12A7 stoichiometric powder was loaded into a graphite crucible with a lid and a melt was formed at 1600 °C in a strongly reducing CO/CO₂ atmosphere similar to the extraction method described in the previous section. When the melt was cooled, it crystallized in the C12A7 decomposition products, C3A and CA, as is expected when no template anions can nucleate crystallization of the cage framework. However, after repeating the process, the melt crystallized into the C12A7 electride suggesting that an anion must be present to nucleate the crystallization of the clathrate framework [29,56]. Raman spectra of the C3A and CA intermediary products revealed an absorption band matched to the reference for CaC₂, however, after the second processing step this absorption band is absent. This is consistent with the notion that the carbide ion decomposes out of the clathrate framework, however, it does not explain why the C12A7 decomposition occurs after the first processing step. Kim et al. report that the electride would seldom form after the initial firing process and is fully reproducible after the second. It is assumed that after the second firing process the carbide ion concentration is high enough to nucleate the full crystallization of the C12A7 electride phase. While this process can be used to directly fabricate melt formed electride single crystals, Kim et al. also show how a glass ceramic can be created by quenching the melt. The quenched melt is transparent and exhibits photochromism as a color change to gray is observed during UV irradiation [10]. The C12A7 crystallization temperature of the glass ceramic was determined to be 900 °C by differential thermal analysis (DTA). After quenching the glass ceramic is sealed in an evacuated quartz tube and fired at 1000 °C for 0.5 h it demonstrated the characteristic green color change and electronic conductivity similar to the melt cooled single crystals.

Recently reduction techniques in an intrinsic carbonaceous environment have been reported. Volodin et al. have developed and extensively studied the functionality of C coatings around TiO₂, MgO, Al₂O₃, and C12A7 nanoparticles [31]. These carbon coatings insulate the nanoparticles from surrounding particles allowing for phase and chemical reactions to occur on the individual particle level through the gas permeable carbon shell at high temperatures while preventing sintering of the nanostructure material. The C coated samples were placed in a graphite crucible sealed in an inert gas purged alumina ampoule and fired at various temperatures between 1250 and 1450 °C for 6 h. Electride formation was observed in all samples. This process closely replicates the CO/CO₂ exchange, albeit at temperatures above the decomposition temperature of 1200 °C observed by Palacios et al. under dry reducing conditions [48]. If the exchange reaction removes the occluded O²⁻ an additional anion would be needed to stabilize the C12A7 framework at these elevated temperatures. Due to this understanding, C₂²⁻ anions must have diffused into the structure from the C coatings, leading to the stability of the clathrate framework at high temperatures.

Chung et al. show that electride formation is possible during spark plasma sintering (SPS) due to the carbonaceous environment [30]. The high localized temperatures, electric field, and plasma all work together to promote diffusion of C species into the C12A7 framework. Graphite dies, which are filled with powdered C12A7, are loaded into an evacuated (1.3×10^{-4} Pa) chamber. The graphite die is necessary to conduct the large amounts of current needed to achieve a ramp rate of 100 °C/min to approximately 1000 °C while having the uniaxial strength to concurrently apply 40 MPa of pressure [30]. The fast ramp rate and short processing time, reported as 0.16 h, leads to fully dense samples with limited sintering [30]. At 900 °C no electride formation occurred, but as the processing temperature was raised to 1000 and 1100 °C electride formation occurred with a higher concentration of localized electrons at 1100 °C [30]. Samples processed at 900 °C were insulating at room temperature while those processed at 1000 °C were still resistive but saw an increase in electrical conductivity with σ_{RT} and n_e of 3.8×10^{-3} S·cm⁻¹ and 3.2×10^{17} , respectively. At a processing temperature of 1100 °C the σ_{RT} and n_e increased to 5.88 S·cm⁻¹ and 5.3×10^{19} , respectively. XRD, of samples processed at 900 and 1000 °C, showed partial decomposition of the C12A7 phase into C3A and CA. Raman spectra of these two samples also show an absorption band corresponding the C₂²⁻ anion. The concentration

of the C_2^{2-} vibrational mode decreases as temperature increases as does the presence of secondary phases. This suggests that the C_2^{2-} vibrational mode is correlated to the decomposition of C12A7 phase. The authors present the hypothesis that these secondary phases recrystallize into C12A7 with C_2^{2-} as the anion responsible for nucleating the clathrate framework. From this point they follow the same argument that the anion is only metastable and decomposes into 2C solid or it reacts with remaining occluded O^{2-} to produce 2CO gas.

We performed similar experiments by sintering sol-gel synthesized C12A7 in a graphite die, similar to the die used in SPS, under high vacuum (10^{-5} Pa). The furnace was ramped at $8^\circ\text{C}/\text{min}$ to 1000, 1200, or 1300 $^\circ\text{C}$ and then held for 2 h. In the 1000 $^\circ\text{C}$ sample, there was limited sintering, no observed color change, and powder XRD shows single phase mayenite. At 1200 $^\circ\text{C}$, the sample showed only slight green/yellow discoloring on the edges of the pellet and powder XRD show (Figure 7) the decomposition products C5A3 and C3A, the same decomposition products observed by Palacios et al. [48]. Another sample was processed at 1200 $^\circ\text{C}$ for 240 h. The resulting pellet, when cross-sectioned, revealed a white core and black edges near the graphite, Figure 7 inset. If the black edges are reduced C12A7 then an anion must be present which can stabilize the framework and it appears to be diffusing from the graphite foil around the powder indicating a C species. At 1300 $^\circ\text{C}$ there was no decomposition of the C12A7 structure and $[\text{Ca}_{24}\text{Al}_{28}\text{O}_{64}]^{4+}:(4 * \delta)e^-(2 - \delta)\text{O}^{2-}$ was formed, confirmed by the observed color change with process duration, changes in relative peak intensity observed through XRD, and Rietveld analysis showed no occluded position occupancy.

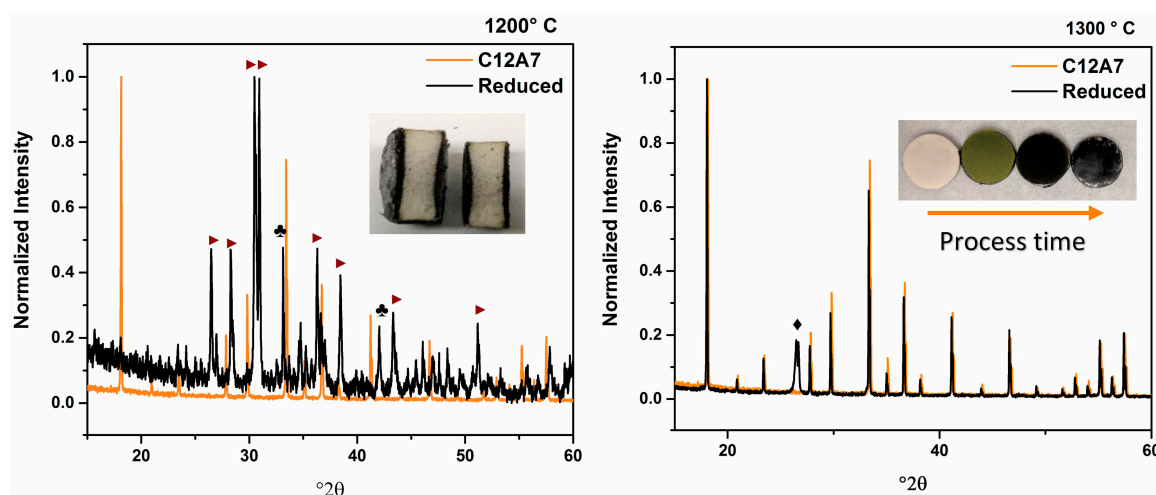


Figure 7. XRD data of vacuum sintered C12A7 in a carbonaceous environment at: 1200 $^\circ\text{C}$ (left); and 1300 $^\circ\text{C}$ (right). The reduced products at 1200 $^\circ\text{C}$ correspond to C3A (\blacklozenge) and C5A3 (\blacktriangle). The inset on the left shows the cross-sectioned pellet demonstrating the diffusion of C species and the inset on the right demonstrates the color change associated with the formation of semiconducting and metallic C12A7. The (\blacklozenge) phase corresponds to graphite foil remaining on the sample surface.

These studies, especially the peculiar nature of the crystallization from the high temperature melt, suggest that a carbonaceous species are able to nucleate the C12A7 structure from the decomposition products of C12A7. What is not clear is if this process only occurs from the decomposition products or if the carbide anion can stabilize the already formed framework structure without decomposition.

O^{2-} , C_2^{2-} , and H^- are primarily the anions reported to form $[\text{Ca}_{24}\text{Al}_{28}\text{O}_{64}]^{4+}:4e^-$. Other reports of electride formation are contributed to induced anion vacancies, however, these vacancies were reported to be small and large scale extraction is not reported. Polfus et al. found an increase in electrical conductivity tied to occluded position and framework vacancies created by outgassing of NH_2^- and N^{3-} under reducing conditions at 700 $^\circ\text{C}$ [28]. Dong et al. reported that, after SPS of isostructural $[\text{Sr}_{24}\text{Al}_{28}\text{O}_{64}]^{4+}:4\text{Cl}^-$ (discussed later), a color change to brown and observed EPR signal

are characteristic of localized F^+ centers [79]. Future research should determine if electrone formation is possible through the removal of the numerous other anions.

4. Cationic Doping of $[Ca_{24}Al_{28}O_{64}]^{4+}:(4 \cdot \delta)e^- (2 - \delta)O^{2-}$

The mineral mayenite forms a supergroup of minerals containing both isostructural oxides and silicates. Gfellar in his review goes in-depth into the different types and synthesis of various group members, especially Cl-mayenite structures, where the cation frameworks, consisting of Mg, Al, Si, Fe, and Ca, are stabilized by Cl^- anions occluded in the cages [44,80]. Research into other doped isostructural compounds has focused on increasing occluded anion occupancy, ion conduction, and luminescent properties. These studies have synthesized a wide variety of stoichiometric structures with aliovalent and isovalent dopants on cationic sites. Known synthetic doped-C12A7 compounds are summarized in Table 2.

Table 2. Isostructural synthesized C12A7 with dopant ionic radii, coordination number (CN), ionic radii (IR), observed dopant concentrations, available lattice parameters, and electrone references (ER).

Dopant + (Co-Dopants) (valence/CN/IR)	Formula Representing the dopant site and change in cage charge with aliovalent doping. The occluded species is not corrected for an increase in cage charge.	References Doped/co-doped C12A7 synthesis	Sub. Site Substitutional site for dopant normally determined by ionic radii	Max x/y Maximum stoichiometric value reported	a [Å]	ER
Oxides						
Sr (2+/6/1.18)	$[Sr_{24}Al_{28}O_{64}]^{4+}; 2O^{2-}$ $[Sr_{24}Al_{28}O_{64}]^{4+}; 4Cl^-$ $[Ca_xSr_{24-x}Al_{28}O_{64}]^{4+}; 2O^{2-}$	[81]—SG ¹ [82]—SS ² [83]—HSS ³ [79]—SS [79]—SPS ⁴ [84]	Ca ²⁺ **	0.24	12.33: (O ²⁻) [83] 12.346 (2): (Cl ₂ ⁻) [79]	[74] [85]
Fe (2+/4/0.63) (2+/6/0.78) (3+/4/0.49) (3+/6/0.645)	$[Ca_{24}Al_{28-x}Fe_xO_{64}]^{4+}; 2O^{2-}$	[15]—SS [75]—FZ ⁵ [86]—FZ [87]—SG	Al ³⁺ **	0.28	11.9904 (4) [75]	[75]
Cu (1+/4/0.6) (1+/6/0.77) (2+/4/0.57) (2+/6/0.73)	$[Ca_{124-x}Cu_xAl_{28}O_{64}]^{4+}; 2O^{2-}$	[88]—SS [87]—SG	Ca ²⁺ **	1	11.974	N/A
Nb (3+/6/0.72) (4+/6/0.68) (5+/4/0.48) (5+/6/0.64)	$[Ca_{24}Al_{28-x}Nb_xO_{64}]^{4+2x+}; 2O^{2-}$	[87]—SG	Al ³⁺	0.24	12.0049(3)	N/A
Ta (3+/6/0.72) (4+/6/0.68) (5+/6/0.64)	$[Ca_{24-x}Ta_xAl_{28}O_{64}]^{4+2x+}; 2O^{2-}$	[87]—SG	Ca ²⁺	0.24	N/A	N/A
Co (2+/4/0.58) (2+/6/0.7) (3+/6/0.58) (4+/4/0.4)	$[Ca_{24}Al_{28}O_{64}Co_x]^{4+}; 2O^{2-}$	[87]—SG	unknown	0.24	N/A	N/A
V (2+/6/0.79) (3+/6/0.64) (4+/6/0.58) (5+/4/0.46) (5+/6/0.54)	$[Ca_{24}Al_{28-x}V_xO_{64}]^{4+2x+}; 2O^{2-}$	[87]—SG	Al ³⁺	0.72-1.2	N/A	N/A
Ni (2+/4/0.55) (2+/6/0.69) (3+/6/0.58) (4+/6/0.48)	$[Ca_{24}Al_{28-x}Ni_xO_{64}]^{4+x+}; 2O^{2-}$	[86]—FZ [87]—SG	Al ³⁺ **	0.28	N/A	N/A
Mg (2+/4/0.57) (2+/6/0.72)	$[Ca_{24-x}Mg_xAl_{28}O_{64}]^{4+}; 2O^{2-}$	[78]—SS [87]—SG	Ca ²⁺	2	N/A	[78]
Dopant + (Co-Dopants) (valence/CN/IR)	Formula	Reference	Sub. Site	Max x/y	a [Å]	ER

Table 2. Cont.

Dopant + (Co-Dopants) (valence/CN/IR)	Formula	References Doped/co-doped C12A7 synthesis	Sub. Site Substitutional site for dopant normally determined by ionic radii	Max x/y Maximum stoichiometric value reported	a [Å]	ER
Al (3+/4/0.39)	Representing the dopant site and change in cage charge with aliovalent doping. The occluded species is not corrected for an increase in cage charge.					
Ca (2+/6/1.00)						
Mn (2+/4/0.66) (2+/6/~0.75) (3+/6/0.65) (4+/4/0.39) (4+/6/0.53) (5+/4/0.33) (6+/4/0.25)	[Ca _{24-x} Mn _x Al ₂₈ O ₆₄] ⁴⁺ :2O ²⁻ [Ca _{24-x} Mn _x Al ₂₈ O ₆₄] ⁴⁺ :4Cl ⁻	[89]—SS [15]—SS	Ca ²⁺ possibly Al ³⁺	0.28	N/A	N/A
Ga (3+/4/0.47) (3+/6/0.62)	[Ca ₂₄ Al _{28-x} Ga _x O ₆₄] ⁴⁺ :2O ²⁻	[90]—SS [87]—SG	Al ³⁺ **	2	11.99734(6)	[90]
Zn + P (2+/4/0.6) (2+/6/0.74)	[Ca ₂₄ Al _{28-x} Zn _x O ₆₄] ^{4-x+} :2O ²⁻	[91]—SS [87]—SG	Al ³⁺	1.3	11.993(2)	N/A
P (3+/6/0.44) (5+/4/0.17) (5+/6/0.38)	[Ca ₂₄ Al _{28-x} P _x O ₆₄] ^{4+2x+} :2O ²⁻	[91]—SS	Al ³⁺	0.66	11.981(2)	N/A
Eu + (Mn, Yb, Nb) (2+/6/1.17) (3+/6/~0.947)	[Ca _{24-x} Eu _x Al ₁₄ O ₆₄] ⁴⁺ :2O ²⁻	[89]—SS [92]—PLD ⁶ [93]—SS [94]—SS [95]	Ca ²⁺	0.04	N/A	N/A
Er (3+/6/0.89)	[Ca _{24-x} Er _x Al ₂₈ O ₆₄] ^{4+x+} :2O ²⁻	[96]—CP ⁷ [94]—SS [95] [97]—CP [98]—SS [98]—SG [99]—SS [95] [100]—SS	Ca ²⁺	0.12 0.72 [94] 2.4 [97]	N/A	N/A
Ce (3+/6/1.01) (4+/6/0.87)	[Ca _{24-x} Ce _x Al ₂₈ O ₆₄] ^{4+x+} :2O ²⁻	[98]—SS [98]—SG [99]—SS [95] [100]—SS	Ca ²⁺	0.24	N/A	N/A
Dy + (Ce) (3+/6/1.07) (4+/6/0.912)	[Ca _{24-x} Dy _x Al ₂₈ O ₃₂] ^{4+x+} :2O ²⁻	[101]—CP [102]	Ca ²⁺	0.48	N/A	N/A
Gd + (Sr) (3+/6/0.938)	[Ca _{24-x} Gd _x Al ₂₈ O ₆₄] ^{4+x+} :2O ²⁻	[103]—SS [95]	Ca ²⁺	0.024	N/A	[103]
Tb + (Ce) (3+/6/0.923) (4+/6/0.76)	[Ca _{24-x} Tb _x Al ₂₈ O ₆₄] ^{4+x+} :2O ²⁻	[99]—SS	Ca ²⁺	0.24	N/A	N/A
Nd (3+/6/0.983)	[Ca _{24-x} Nd _x Al ₂₈ O ₆₄] ^{4+x+} :2O ²⁻	[93]—SS [72]—FZ	Ca ²⁺	0.2	N/A	N/A
Dopant + (Co-Dopants) (valence/CN/IR)	Formula	Reference	Sub. Site	Max x/y	a [Å]	ER
Yb (2+/6/1.02) (3+/6/0.868)	[Ca _{24-x} Yb _x Al ₂₈ O ₆₄] ^{4+x+} :2O ²⁻	[94]—SS	Ca ²⁺	2.4	N/A	N/A
Ho (3+/6/0.901)	[Ca _{24-x} Ho _x Al ₂₈ O ₆₄] ^{4+x+} :2O ²⁻	[104]—CP [97]—CP	Ca ²⁺	1.2	N/A	N/A
Pr (3+/6/0.99) (4+/6/0.85)	[Ca _{24-x} Pr _x Al ₂₈ O ₆₄] ^{4+x+} :2O ²⁻	[105]—SS	Ca ²⁺	0.192	12.007	N/A
Sm (3+/6/0.958)	[Ca _{24-x} Sm _x Al ₂₈ O ₆₄] ^{4+x+} :2O ²⁻	[106]—SG	Ca ²⁺	0.48	N/A	[106]
Silicates						
Si (4+/4/0.26) (4+/6/0.4)	[Ca ₂₄ Al ₂₀ Si ₈ O ₆₄] ¹²⁺ :6O ²⁻	[16]—HT ⁸ [54]—HT [107]—HT	Al ³⁺ **	-	11.9748 (15) [16]	[54]
Fe + Si	[Ca ₂₄ Fe ₂₀ Si ₈ O ₆₄] ¹²⁺ :12Cl ⁻	[108]—SS	Al ³⁺ **	-	12.2158 (8)	N/A
Si + (Co, Ni, Cr, Cu, Fe)	[Ca _{24-y} X _y Al ₂₀ Si ₈ O ₆₄] ¹²⁺ :6O ²⁻	[109]—HT [107]—HT [110]—HT(Co)	Ca ²⁺	Cu (1.2) Cr (1.7) Co (0.82) Ni (2.4) Fe (0.96)	N/A	N/A

** Empirical confirmation; ¹ SG—Sol-Gel synthesis; ² SS—solid state synthesis; ³ HSS—High pressure solid state synthesis; ⁴ SPS—Spark Plasma Synthesis; ⁵ FZ—Float Zone Single Crystal synthesis; ⁶ PLD—Pulsed Laser Deposition synthesis; ⁷ CP—Co-Precipitation synthesis; ⁸ HT—Hydrothermal synthesis; Highlighted ionic radii information is the observed or expected coordination of dopant. All Ionic radii information is from [111].

The amount of research into the electroneutral properties of doped-C12A7 is lacking in comparison to research on oxygen conduction and luminescence. Electroneutral investigations of S12A7, an isostructural compound with 100% substitution of Sr for the Ca, was performed by Hosono's group who evaluated

S12A7 thin films to see if they exhibited the same electrider features as C12A7. Electrider formation was confirmed through two reduction processes, H^- ion implantation and oxygen deficient amorphous C12A7. After UV irradiation, the implanted thin films exhibited similar conductivities, activation energy, temperature dependence, and absorption behavior as electrider C12A7. The oxygen deficient reduction process led to a conductivity of approximately $270 \text{ S}\cdot\text{cm}^{-1}$ and an electron concentration of 1.3×10^{21} . Physical property measurements coupled with a Drude effect in the optical absorption spectra confirms that S12A7 exhibits similar conductivity mode changes associated with the metal to insulator transition (MIT) of C12A7 [74]. Further studies of layered C12A7/S12A7 thin films found an increase in carrier mobility possibly associated with accumulation of charge carriers at the interface between the two films [85].

Bertoni et al. studied the possibility of $[\text{Ca}_{24}\text{Al}_{20}\text{Si}_8\text{O}_{64}]^{12+}$ being a transparent conductive oxide and induced electrider formation through the H^- replacement reduction process [54]. Hydrogarnet was calcined at 800°C to form the C12A7 compound, however, it is reported that samples decomposed at elevated temperatures and hydrogen incorporation by the conventional route was not possible. Instead H^- replacement was conducted at 300°C through ion implantation. They found that the electrical conductivity double and tripled with increasing Si doping. Further it was found that a slight increase in Seebeck coefficient was observed with increasing dopant concentration and the sign remained negative as expected when below the MIT. Bertoni et al. stress that the increase in conductivity is primarily due to an increase in available hopping centers and not due to the gradual increase in electron concentrations associated with an increase in H^- [54]. Only low electron concentration electrideres were formed and due to the metastability of the phase there is currently no process to fully reduce $[\text{Ca}_{24}\text{Al}_{20}\text{Si}_8\text{O}_{64}]^{12+}$ to the metallic regime. Bertoni et al. also studied $[\text{Ca}_{23.76}\text{Mg}_{0.24}\text{Al}_{28}\text{O}_{64}]^{4+}$ electrider reduced by H^- replacement process and found that conductivity decreased with increasing Mg concentration due to Mg acting as a blocking agent for hopping conductivity [78]. These two studies illuminate that in the semiconducting regime hopping sites and not carrier concentration limits electrical conductivity.

Palacios et al. studied the electrider formation of $[\text{Ca}_{24}\text{Al}_{26}\text{Gd}_2\text{O}_{64}]^{4+}$. The lattice parameter increased to $11.99734(6) \text{ \AA}$. The samples were then reduced by firing pellets in an alumina crucible buried in graphite powder at 1350°C for 6 h. The resultant gray pellet was multiphase with C3A phase in high concentrations. Structural refinements revealed that the lattice parameter of the reduced sample was close to 11.989 \AA , close to the lattice parameter of undoped stoichiometric C12A7, and the Ga site occupancy refined to zero. Further X-ray photoelectron spectroscopy (XPS) revealed that the Ga^{3+} reduced to Ga metal and the conclusion was drawn that this metal must be nanodispersed on the C12A7 surface [90]. This study raises concern of the stability of doped C12A7 under reducing conditions, especially when considering transition metals that may change oxidation states under reducing conditions.

Ali et al. performed the Ti reduction process on blue colored 0.1 mol % Nd aliovalent doped C12A7 FZ single crystals [72]. Maximum electrical conductivity values were lower than those reported by Kim et al. and carrier mobility and concentration were measured via Hall measurements yielding large errors [57]. Ali et al. found that carrier mobility increases with annealing time while carrier concentration is independent of annealing time between 36 and 60 h. Further, when compared to undoped C12A7 at the same annealing time and temperature Ali et al. found an increase in carrier concentration with similar carrier mobility, and low temperature carrier mobility was higher in the doped case [72]. This is the first electrider investigation of aliovalent doped C12A7 and shows an increase in carrier density and mobility from the undoped C12A7.

Since the CCB is responsible for electrical conductivity in C12A7, modifications to the chemical species in cage framework can have profound impacts on the landscape of DOS around the Fermi energy, leading to changes in electron localization, electrical conductivity, and Seebeck coefficient. Huang et al. performed DFT and electron localization function (ELF) calculations to investigate the change in DOS of the CCB and the change in attractive anionic species with various cation dopants.

They modeled the stoichiometric and fully reduced electrified structures doped with ~0.86 mol % of Cu, Sr, Fe, Ir, P, and V [34]. Lattice parameter had a linear trend with ionic radii validating the qualitative assessment of dopant substitution and substitutional site normally employed by experimental investigation. Cu, Fe, and Ir are exceptions to this rule suggesting an increase in cage distortion with respect to other studied dopants. As the electrified is formed the lattice parameter increases by approximately 0.03 Å for all dopants except for Fe, where the lattice parameter only increases about 0.01 Å [34].

Density of state calculations confirm the assumption that small changes in the cage framework can drastically alter the density of states around the Fermi level, shown in Figure 8. Transition metal dopants lead to an increase in interstitial states in the stoichiometric case, which disappear as the electrified is formed. At maximum electron loading Ir and Cu lead to occupied states at the Fermi level contrasted to the valley observed in the stoichiometric case, shown in Figure 4, and other dopant cases. In Cu-doped C12A7 the DOS of the CCB decreases from the stoichiometric to the electrified case further suggesting a distortion of the cage framework.

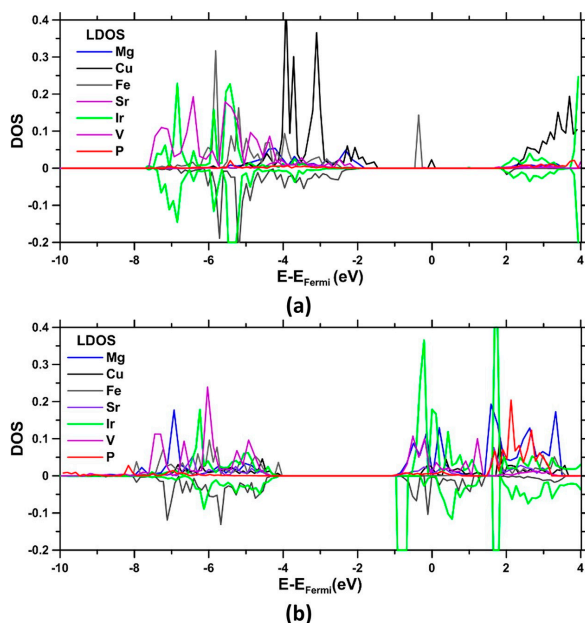


Figure 8. Local DOS with respect to dopant in (a) C12A7 and (b) C12A7 electrified. Reprinted with permission from [34]. Copyright 2015 American Chemical Society.

Electron localization function calculations are used to analyze chemical bonds and the localization of anionic species in C12A7. Huang et al. found the character of the occluded species, localization of the electron, and distortion of the C12A7 framework varies based on dopant. If the presence of a localized F^+ like center electron indicates semiconducting hopping conduction and the absence of this localized attractor is characteristic of delocalized band conduction then Mg, Sr, P, and V exhibit a semiconducting state while Cu, Ir, and Fe exhibit band conduction at max electron concentration. This assumption is unclear as undoped-C12A7 shows a strong F^+ attractor, however previous investigations have shown that the dominant conduction carrier is a free carrier when fully reduced. The presence of localized attractors in the ELF calculations does align with the observation by Lobo et al. where increasing carrier concentration ultimately leads to an increase in lattice electron coupling observed in undoped C12A7. Will the increase in Fano effect be observed for Cu, Ir, and Fe doped systems? Does the distortion to the framework negate the formation of polarons at high electron loading like in other systems? For Mg doping a stronger attraction to the F^+ center than in undoped C12A7 confirms the

theoretical and experimental results found by Bertoni et al. that Mg acts as a blocking agent in the hopping conduction regime [78].

Cationic dopants are theoretically predicted to have profound impacts on the structure and electrical properties of $[\text{Ca}_{24}\text{Al}_{28}\text{O}_{64}]^{4+} \cdot 4\text{e}^-$. Investigations into the effects of these dopants are few and research should proceed to quantify and confirm the effects dopants will have on the Seebeck coefficient, electrical conductivity, and superconducting transition. What is unclear is the experimental stability of the cation doped framework both during the process to extract or replace the occluded anions and in the final electride state.

5. Conclusions

$[\text{Ca}_{24}\text{Al}_{28}\text{O}_{64}]^{4+} \cdot (4 * \delta)\text{e}^- (2 - \delta)\text{O}^{2-}$ consists of a clathrate cage framework whose complicated crystallographic structure results in interesting properties with potential applications in both the stoichiometric and electride states. The convertibility from a wide band gap insulator to semiconductor to metallic conductor is performed through processing without the need for acceptor and donor dopants as with traditional semiconductors. The strong atomic structure to physical property relationship is responsible for this transition and modifying this structure leads to a transformation of the electronic density of states. The intricacies of the mayenite structure are far from solved and future research is still needed. Some areas for future investigations are:

1. Determining what is responsible for the increase in the Fano effect with increased carrier concentration and what is the relationship between free carriers and polarons.
2. Synthesis of new doped-isostructural compounds and subsequent characterization of the structural and electronic changes that occur.
3. Development of new reduction processes for Cl^- stabilized structure that will be stable at higher temperatures and have large substitutions of framework Ca and Al cations.
4. Development of direct electride synthesis processes where the cage framework can be nucleated by e^- or through an anion exchange process where, after the framework nucleates slight changes in synthesis conditions, the stabilizing anions can be extracted creating anionic vacancies.

Acknowledgments: The authors would like to acknowledge funding from the State of Tennessee and Tennessee Higher Education Commission (THEC) through their support of the Center for Materials Processing. The authors would also like to thank Bryan Chakoumakos from Oak Ridge National Laboratory for his comments and suggestions.

Author Contributions: John Robert Salasin performed the experiments; John Robert Salasin and Claudia Rawn analyzed the data; and John Robert Salasin and Claudia Rawn wrote the paper.

Conflicts of Interest: The authors declare no conflict of interest.

References

1. Boysen, H.; Lerch, M.; Stys, A.; Senyshyn, A. Structure and oxygen mobility in mayenite ($\text{Ca}_{12}\text{Al}_{14}\text{O}_{33}$): A high-temperature neutron powder diffraction study. *Acta Crystallogr. Sect. B Struct. Sci.* **2007**, *B63*, 675–682. [[CrossRef](#)] [[PubMed](#)]
2. Kim, S.W.; Hosono, H. Synthesis and properties of $12\text{CaO} \cdot 7\text{Al}_2\text{O}_3$ electride: Review of single crystal and thin film growth. *Philos. Mag.* **2012**, *92*, 2596–2628. [[CrossRef](#)]
3. Sushko, P.V.; Shluger, A.L.; Hirano, M.; Hosono, H. From Insulator to Electride: A Theoretical Model of Nanoporous Oxide $12\text{CaO} \cdot 7\text{Al}_2\text{O}_3$. *J. Am. Chem. Soc.* **2007**, *129*, 942–951. [[CrossRef](#)] [[PubMed](#)]
4. Zhmoidin, G.I.; Chatterjee, A.K. Conditions and mechanism of interconvertibility of compounds $12\text{CaO} \cdot 7\text{Al}_2\text{O}_3$ and $5\text{CaO} \cdot 3\text{Al}_2\text{O}_3$. *Cem. Concr. Res.* **1984**, *14*, 386–396. [[CrossRef](#)]
5. Teusner, M.; De Souza, R.A.; Krause, H.; Ebbinghaus, S.G.; Belghoul, B.; Martin, M. Oxygen Diffusion in Mayenite. *J. Phys. Chem. C* **2015**, *119*, 9721–9727. [[CrossRef](#)]
6. Hayashi, K.; Hirano, M.; Hosono, H. Thermodynamics and Kinetics of Hydroxide Ion Formation in $12\text{CaO} \cdot 7\text{Al}_2\text{O}_3$. *J. Phys. Chem. B* **2005**, *109*, 11900–11906. [[CrossRef](#)] [[PubMed](#)]

7. Edmonds, R.N.; Majumdar, A.J. The hydration of $12\text{CaO} \cdot 7\text{Al}_2\text{O}_3$ at different temperatures. *Cem. Concr. Res.* **1988**, *18*, 473–478. [[CrossRef](#)]
8. Hayashi, K.; Sushko, P.V.; Ramo, D.M.; Shluger, A.L.; Watauchi, S.; Tanaka, I.; Matsuishi, S.; Hirano, M.; Hosono, H. Nanoporous Crystal $12\text{CaO} \cdot 7\text{Al}_2\text{O}_3$: A Playground for Studies of Ultraviolet Optical Absorption of Negative Ions. *J. Phys. Chem. B* **2007**, *111*, 1946–1956. [[CrossRef](#)] [[PubMed](#)]
9. Eufinger, J.-P.; Schmidt, A.; Lerch, M.; Janek, J. Novel anion conductors—Conductivity, thermodynamic stability and hydration of anion-substituted mayenite-type cage compounds $\text{C}_{12}\text{A}_7\text{X}$ (X = O, OH, Cl, F, CN, S, N). *Phys. Chem. Chem. Phys.* **2015**, *17*, 6844–6857. [[CrossRef](#)] [[PubMed](#)]
10. Hayashi, K.; Hirano, M.; Matsuishi, S.; Hosono, H. Microporous crystal $12\text{CaO} \cdot 7\text{Al}_2\text{O}_3$ encaging abundant O- radicals. *J. Am. Chem. Soc.* **2002**, *124*, 738–739. [[CrossRef](#)] [[PubMed](#)]
11. Hayashi, K.; Hirano, M.; Li, Q.-X.; Nishioka, M.; Sadakata, M.; Torimoto, Y.; Matsuishi, S.; Hosono, H. Electric Field Emission of High Density O- Ions from $12\text{CaO} \cdot 7\text{Al}_2\text{O}_3$ Engineered to Incorporate Oxygen Radicals. *Electrochem. Solid State Lett.* **2002**, *5*, J13–J16. [[CrossRef](#)]
12. Hayashi, K.; Matsuishi, S.; Ueda, N.; Hirano, M.; Hosono, H. Maximum Incorporation of Oxygen Radicals, O- and O₂⁻, into $12\text{CaO} \cdot 7\text{Al}_2\text{O}_3$ with a Nanoporous Structure. *Chem. Mater.* **2003**, *15*, 1851–1854. [[CrossRef](#)]
13. Hayashi, K.; Ueda, N.; Hirano, M.; Hosono, H. Effect of stability and diffusivity of extra-framework oxygen species on the formation of oxygen radicals in $12\text{CaO} \cdot 7\text{Al}_2\text{O}_3$. *Solid State Ion.* **2004**, *173*, 89–94. [[CrossRef](#)]
14. Yang, S.; Kondo, J.N.; Hayashi, K.; Hirano, M.; Domen, K.; Hosono, H. Formation and Desorption of Oxygen Species in Nanoporous Crystal $12\text{CaO} \cdot 7\text{Al}_2\text{O}_3$. *Chem. Mater.* **2004**, *16*, 104–110. [[CrossRef](#)]
15. Stober, R.; Nofz, M.; Gesner, W.; Kranz, G. Paramagnetic monitors (Mn^{2+} , Mn^{4+} , Fe^{3+} , and O^{2-}) in the solid-state reaction yielding $12\text{CaO} \cdot 7\text{Al}_2\text{O}_3$ and other aluminates. *J. Solid State Chem.* **1989**, *81*, 152–164. [[CrossRef](#)]
16. Fujita, S.; Suzuki, K.; Ohkawa, M.; Mori, T.; Iida, Y.; Youhei, M.; Hideki, M.; Shimada, S. Oxidative Destruction of Hydrocarbons on a New Zeolite-like Crystal of $\text{Ca}_{12}\text{Al}_{10}\text{Si}_4\text{O}_{35}$ Including O₂⁻ and O₂²⁻-Radicals. *Chem. Mater.* **2003**, *15*, 255–263. [[CrossRef](#)]
17. Hayashi, K.; Hirano, M.; Hosono, H. Excess Oxygen in $12\text{CaO} \cdot 7\text{Al}_2\text{O}_3$ Studied by Thermogravimetric Analysis. *Chem. Lett.* **2005**, *34*, 586–587. [[CrossRef](#)]
18. Sushko, P.V.; Shluger, A.L.; Hayashi, K.; Hirano, M.; Hosono, H. Role of hydrogen atoms in the photoinduced formation of stable electron centers in H-doped $12\text{CaO} \cdot 7\text{Al}_2\text{O}_3$. *Phys. Rev. B* **2006**, *73*. [[CrossRef](#)]
19. Hayashi, K.; Hirano, M.; Hosono, H. Functionalities of a nanoporous crystal $12\text{CaO} \cdot 7\text{Al}_2\text{O}_3$ originating from the incorporation of active anions. *Bull. Chem. Soc. Jpn.* **2007**, *80*, 872–884. [[CrossRef](#)]
20. Hayashi, K. Kinetics of electron decay in hydride ion-doped mayenite. *J. Phys. Chem. C* **2011**, *115*, 11003–11009. [[CrossRef](#)]
21. Hayashi, K.; Matsuishi, S.; Kamiya, T.; Hirano, M.; Hosono, H. Light-induced conversion of an insulating refractory oxide into a persistent electronic conductor. *Nature* **2002**, *419*, 462–465. [[CrossRef](#)] [[PubMed](#)]
22. Jeevaratnam, J.; Glasser, F.P.; Glasser, L.S.D. Anion Substitution and Structure of $12\text{CaO} \cdot 7\text{Al}_2\text{O}_3$. *J. Am. Ceram. Soc.* **1964**, *47*, 105–106. [[CrossRef](#)]
23. Williams, P.P. Refinement of the structure of $11\text{CaO} \cdot 7\text{Al}_2\text{O}_3 \cdot \text{CaF}_2$. *Acta Cryst.* **1973**, *B29*, 1550–1551. [[CrossRef](#)]
24. Song, C.; Sun, J.; Li, J.; Ning, S.; Yamamoto, M.; Tu, J.; Torimoto, Y.; Li, Q. Characteristics and Mechanisms of atomic fluorine anions emission from nanoporous crystal $[\text{Ca}_{24}\text{Al}_{28}\text{O}_{64}]^{4+}(\text{F}^-)_{3.36}(\text{O}^{2-})_{0.32}$ Surface. *J. Phys. Chem. C* **2008**, *112*, 19061–19068. [[CrossRef](#)]
25. Feng, Q.L.; Glasser, F.P.; Howie, R.A.; Lachowski, E.E. Chlorosilicate with the $12\text{CaO} \cdot 7\text{Al}_2\text{O}_3$ structure and its relationship to garnet. *Acta Cryst.* **1988**, *C44*, 589–592. [[CrossRef](#)]
26. Schmidt, A.; Lerch, M.; Eufinger, J.P.; Janek, J.; Dolle, R.; Wiemhöfer, H.D.; Tranca, I.; Islam, M.M.; Bredow, T.; Boysen, H.; et al. CN-mayenite $\text{Ca}_{12}\text{Al}_{14}\text{O}_{32}(\text{CN})_2$: Replacing mobile oxygen ions by cyanide ions. *Solid State Sci.* **2014**, *38*, 69–78. [[CrossRef](#)]
27. Schmidt, A.; Boysen, H.; Senyshyn, A.; Lerch, M. New findings on N-mayenite and a new kind of anion substituted mayenite: $\text{Ca}_{12}\text{Al}_{14}\text{O}_{32}(\text{NO}_2)_2$. *Z. Krist.* **2014**, *229*, 427–434. [[CrossRef](#)]
28. Polfus, J.M.; Toyoura, K.; Hervoches, C.H.; Sunding, M.F.; Tanaka, I.; Haugrud, R. Nitrogen and hydrogen defect equilibria in $\text{Ca}_{12}\text{Al}_{14}\text{O}_{33}$: A combined experimental and computational study. *J. Mater. Chem.* **2012**, *22*, 15828–15835. [[CrossRef](#)]

29. Kim, S.; Miyakawa, M.; Hayashi, K.; Sakai, T.; Hirano, M.; Hosono, H. Simple and Efficient Fabrication of Room Temperature Stable Electride: Melt-Solidification and Glass Ceramics. *J. Am. Chem. Soc.* **2005**, *127*, 1370–1371. [[CrossRef](#)] [[PubMed](#)]
30. Chung, J.H.; Ryu, J.H.; Eun, J.W.; Choi, B.G.; Shim, K.B. One-Step Synthesis of a $12\text{CaO} \cdot 7\text{Al}_2\text{O}_3$ Electride via the Spark Plasma Sintering (SPS) Method. *Electrochem. Solid-State Lett.* **2011**, *14*, E41–E43. [[CrossRef](#)]
31. Volodin, A.M.; Zaikovskii, V.I.; Kenzhin, R.M.; Bedilo, A.F.; Mishakov, I.V.; Vedyagin, A.A. Synthesis of Nanocrystalline Calcium Aluminate C12A7 under Carbon Nanoreactor Conditions. *Mater. Lett.* **2017**, *189*, 210–212. [[CrossRef](#)]
32. Boysen, H.; Kaiser-Bishoff, I.; Lerch, M. Anion Diffusion Processes in O- and N-Mayenite Investigated by Neutron Powder Diffraction. *Diffus. Fundam.* **2008**, *8*, 2.1–2.8.
33. Miyakawa, M.; Kamioka, H.; Hirano, M.; Kamiya, T.; Sushko, P.V.; Shluger, A.L.; Matsunami, N.; Hosono, H. Photoluminescence from Au ion-implanted nanoporous single-crystal $12\text{CaO} \cdot 7\text{Al}_2\text{O}_3$. *Phys. Rev. B* **2006**, *73*. [[CrossRef](#)]
34. Huang, J.; Valenzano, L.; Sant, G. Framework and Channel Modifications in Mayenite ($12\text{CaO} \cdot 7\text{Al}_2\text{O}_3$) Nanocages By Cationic Doping. *Chem. Mater.* **2015**, *27*, 4731–4741. [[CrossRef](#)]
35. Bridges, F.; Davies, G.; Robertson, J.; Stoneham, A.M. The spectroscopy of crystal defects: A compendium of defect nomenclature. *J. Phys. Condens. Matter* **1990**, *2*, 2875–2928. [[CrossRef](#)]
36. Dye, J.L. Electrides: Early Examples of Quantum Confinement. *Acc. Chem. Res.* **2009**, *42*, 1564–1572. [[CrossRef](#)] [[PubMed](#)]
37. Matsuishi, S.; Toda, Y.; Miyakawa, M.; Hayashi, K.; Kamiya, T.; Hirano, M.; Tanaka, I.; Hosono, H. High-density electron anions in a nanoporous single crystal: $[\text{Ca}_{24}\text{Al}_{28}\text{O}_{64}]^{4+}(4e^-)$. *Science* **2003**, *301*, 626–629. [[CrossRef](#)] [[PubMed](#)]
38. Zhang, X.; Xiao, Z.; Lei, H.; Toda, Y.; Matsuishi, S.; Kamiya, T.; Ueda, S.; Hosono, H. Two-dimensional transition-metal electride Y2C. *Chem. Mater.* **2014**, *26*, 6638–6643. [[CrossRef](#)]
39. Lee, K.; Kim, S.W.; Toda, Y.; Matsuishi, S.; Hosono, H. Dicalcium nitride as a two-dimensional electride with an anionic electron layer. *Nature* **2013**, *494*, 336–341. [[CrossRef](#)] [[PubMed](#)]
40. Inoshita, T.; Jeong, S.; Hamada, N.; Hosono, H. Exploration for two-dimensional electrides via database screening and ab initio calculation. *Phys. Rev. X* **2014**, *4*, 031023. [[CrossRef](#)]
41. Zhao, S.; Kan, E.; Li, Z. Electride: From computational characterization to theoretical design. *WIREs Comput. Mol. Sci.* **2016**, *6*, 430–440. [[CrossRef](#)]
42. Liao, S.; Yao, R.; Chen, X.; Wang, G.; Zheng, F. Characteristics, Thermodynamics, and Preparation of Nanocaged $12\text{CaO} \cdot 7\text{Al}_2\text{O}_3$ and Its Derivatives. *Int. J. Appl. Ceram. Technol.* **2016**, *13*, 844–855. [[CrossRef](#)]
43. Kim, S.-W.; Matsuishi, S.; Miyakawa, M.; Hayashi, K.; Hirano, M.; Hosono, H. Fabrication of room temperature-stable $12\text{CaO} \cdot 7\text{Al}_2\text{O}_3$ electride: A review. *J. Mater. Sci. Mater. Electron.* **2007**, *18*, S5–S14. [[CrossRef](#)]
44. Gfellar, F. *Highlights in Mineralogical Crystallography: Mayenite $\text{Ca}_{12}\text{Al}_{14}\text{O}_{33}$: From Minerals to the First Stable Electride Crystals*; Armbruster, T., Danisi, R.M., Eds.; Walter de Gruyter GmbH & Co KG: Berlin, Germany, 2016; ISBN 978-3-11-041704-3.
45. Feizi, E.; Ray, A.K. $12\text{CaO} \cdot 7\text{Al}_2\text{O}_3$ Ceramic: A Review of the Electronic and Optoelectronic Applications in Display Devices. *J. Disp. Technol.* **2016**, *12*, 451–459. [[CrossRef](#)]
46. Sakakura, T.; Tanaka, K.; Takenaka, Y.; Matsuishi, S.; Hosono, H.; Kishimoto, S. Determination of the local structure of a cage with an oxygen ion in $\text{Ca}_{12}\text{Al}_{14}\text{O}_{33}$. *Acta Crystallogr. Sect. B Struct. Sci.* **2011**, *67*, 193–204. [[CrossRef](#)] [[PubMed](#)]
47. Palacios, L.; Cabeza, A.; Bruque, S.; Garcia-Granda, S.; Aranda, M.A.G. Structure and Electrons in Mayenite Electrides. *Inorg. Chem.* **2008**, *47*, 2661–2667. [[CrossRef](#)] [[PubMed](#)]
48. Palacios, L.; De La Torre, Á.G.; Bruque, S.; García-Muñoz, J.L.; García-Granda, S.; Sheptyakov, D.; Aranda, M.A.G. Crystal structures and in-situ formation study of mayenite electrides. *Inorg. Chem.* **2007**, *46*, 4167–4176. [[CrossRef](#)] [[PubMed](#)]
49. Nomura, T.; Hayashi, K.; Kubota, Y.; Kamiya, T.; Hirano, M.; Takata, M.; Hosono, H. Anion Incorporation-induced Cage Deformation in $12\text{CaO} \cdot 7\text{Al}_2\text{O}_3$ Crystal. *Chem. Lett.* **2007**, *36*, 902–903. [[CrossRef](#)]
50. Boysen, H.; Kaiser-Bischoff, I.; Lerch, M.; Berendts, S.; Börger, A.; Trots, D.M.; Hoelzel, M.; Senyshyn, A. Structures and properties of variously doped Mayenite investigated by neutron and synchrotron powder diffraction. *Z. Krist. Suppl.* **2009**, *30*, 323–328. [[CrossRef](#)]

51. Matsuishi, S.; Kim, S.W.; Kamiya, T.; Hirano, M.; Hosono, H. Localized and Delocalized Electrons in Room-Temperature Stable Electride $[\text{Ca}_{24}\text{Al}_{28}\text{O}_{64}]^{4+}(\text{O}^{2-})_{2-x}(\text{e}^-)_{2x}$: Analysis of Optical Reflectance Spectra. *J. Phys. Chem. C* **2008**, *112*, 4753–4760. [[CrossRef](#)]
52. Lobo, R.P.S.M.; Bontemps, N.; Bertoni, M.I.; Mason, T.O.; Poeppelmeier, K.R.; Freeman, A.J.; Park, M.S.; Medvedeva, J.E. Optical Conductivity of Mayenite: From Insulator to Metal. *J. Phys. Chem. C* **2015**, *119*, 8849–8856. [[CrossRef](#)]
53. Medvedeva, J.E.; Freeman, A.J. Combining high conductivity with complete optical transparency: A band-structure approach. *Europhys. Lett.* **2005**, *69*, 583. [[CrossRef](#)]
54. Bertoni, M.I.; Mason, T.O.; Medvedeva, J.E.; Wang, Y.; Freeman, A.J.; Poeppelmeier, K.R. Enhanced electronic conductivity in Si-substituted calcium aluminate. *J. Appl. Phys.* **2007**, *102*, 113704. [[CrossRef](#)]
55. Li, Z.; Yang, J.; Hou, J.G.; Zhu, Q. Is mayenite without clathrated oxygen an inorganic electride? *Angew. Chem. Int. Ed.* **2004**, *43*, 6479–6482. [[CrossRef](#)] [[PubMed](#)]
56. Kim, S.W.; Toda, Y.; Hayashi, K.; Hirano, M.; Hosono, H. Synthesis of a Room Temperature Stable $12\text{CaO} \cdot 7\text{Al}_2\text{O}_3$ Electride from the Melt and Its Application as an Electron Field Emitter. *Chem. Mater.* **2006**, *18*, 1938–1944. [[CrossRef](#)]
57. Kim, S.W.; Matsuishi, S.; Nomura, T.; Kubota, Y.; Takata, M.; Hayashi, K.; Kamiya, T.; Hirano, M.; Hosono, H. Metallic State in a Lime—Alumina Compound with Nanoporous Structure. *Nano Lett.* **2007**, *7*, 1138–1143. [[CrossRef](#)] [[PubMed](#)]
58. Kim, S.W.; Miyakawa, M.; Hirano, M.; Kohama, Y.; Kawaji, H.; Atake, T.; Ikegami, H.; Kono, K.; Hosono, H. Superconducting Transition in Electron-Doped $12\text{CaO} \cdot 7\text{Al}_2\text{O}_3$. *Mater. Trans.* **2008**, *49*, 1748–1752. [[CrossRef](#)]
59. Kim, S.W.; Hayashi, K.; Hirano, M.; Hosono, H.; Tanaka, I. Electron carrier generation in a refractory oxide $12\text{CaO} \cdot 7\text{Al}_2\text{O}_3$ by heating in reducing atmosphere: Conversion from an insulator to a persistent conductor. *J. Am. Ceram. Soc.* **2006**, *89*, 3294–3298. [[CrossRef](#)]
60. Hosono, H.; Kim, S.-W.; Matsuishi, S.; Tanaka, S.; Miyake, A.; Kagayama, T.; Shimizu, K. Superconductivity in room-temperature stable electride and high-pressure phases of alkali metals. *Philos. Trans. A* **2015**, *373*, 20140450. [[CrossRef](#)] [[PubMed](#)]
61. Ebbinghaus, S.G.; Krause, H.; Syrowatka, F. Floating Zone Growth of Large and Defect-free $\text{Ca}_{12}\text{Al}_{14}\text{O}_{33}$ Single Crystals. *Cryst. Growth Des.* **2013**, *13*, 2990–2994. [[CrossRef](#)]
62. Kurashige, K.; Toda, Y.; Matsuishi, S.; Hayashi, K.; Hirano, M.; Hosono, H. Czochralski Growth of $12\text{CaO} \cdot 7\text{Al}_2\text{O}_3$ Crystals. *Cryst. Growth Des.* **2006**, *6*, 1602–1605. [[CrossRef](#)]
63. Tian, Y.; Pan, X.; Yu, H.; Tu, G. Formation mechanism of calcium aluminate compounds based on high-temperature solid-state reaction. *J. Alloys Compd.* **2016**, *670*, 96–104. [[CrossRef](#)]
64. Ruzsak, M.; Witkowski, S.; Pietrzyk, P.; Kotarba, A.; Sojka, Z. The role of intermediate calcium aluminate phases in solid state synthesis of mayenite ($\text{Ca}_{12}\text{Al}_{14}\text{O}_{33}$). *Funct. Mater. Lett.* **2011**, *4*, 183–186. [[CrossRef](#)]
65. Phase Equilibria Diagrams Online Database (NIST Standard Reference Database 31), The American Ceramic Society and the National Institute of Standards and Technology, 2017. Figure Numbers 12337. Available online: www.nist.gov/srd/nist31.cfm (accessed on 10 April 2017).
66. Rashad, M.M.; Mostafa, A.G.; Rayan, D.A. Structural and optical properties of nanocrystalline mayenite $\text{Ca}_{12}\text{Al}_{14}\text{O}_{33}$ powders synthesized using a novel route. *J. Mater. Sci. Mater Electron.* **2016**, *27*, 2614–2623. [[CrossRef](#)]
67. Matsuishi, S.; Nomura, T.; Hirano, M.; Kodama, K.; Shamoto, S.I.; Hosono, H. Direct synthesis of powdery inorganic electride $[\text{Ca}_{24}\text{Al}_{28}\text{O}_{64}]^{4+}(\text{e}^-)_4$ and determination of oxygen stoichiometry. *Chem. Mater.* **2009**, *21*, 2589–2591. [[CrossRef](#)]
68. Inoue, Y.; Kitano, M.; Kim, S.-W.; Yokoyama, T.; Hara, M.; Hosono, H. Highly Dispersed Ru on Electride $[\text{Ca}_{24}\text{Al}_{28}\text{O}_{64}]^{4+}(\text{e}^-)_4$ as a Catalyst for Ammonia Synthesis. *ACS Catal.* **2014**, *4*, 674–680. [[CrossRef](#)]
69. Yoon, S.G.; Kim, S.W.; Yoon, D.H.; Hirano, M.; Hosono, H. Single crystal growth of nanoporous $\text{C}_{12}\text{A}_7\text{:e}^-$ by controlling melt state. *J. Nanosci. Nanotechnol.* **2009**, *9*, 7345–7349. [[CrossRef](#)] [[PubMed](#)]
70. Kofstad, P. Thermogravimetric Studies of the Defect Structure of Rutile (TiO_2). *J. Phys. Chem. Solids* **1962**, *23*, 1579–1586. [[CrossRef](#)]
71. Jacob, K.T.; Rajitha, G. Gibbs Energy of Formation of $\text{Ca}_3\text{Ti}_8\text{Al}_{12}\text{O}_{37}$ and Phase Relations and Chemical Potentials in the System Al_2O_3 - TiO_2 - CaO . *J. Phase Equilibria Diffus.* **2012**, *33*, 293–302. [[CrossRef](#)]
72. Ali, M.M.; Nagao, M.; Watauchi, S.; Tanaka, I. Floating Zone Growth and Characterization of $(\text{Ca}_{1-x}\text{Nd}_x)_{12}\text{Al}_{14}\text{O}_{33+6x}$ ($x=0.001$) Single Crystals. *ACS Omega* **2016**, *1*, 1157–1163. [[CrossRef](#)]

73. Miyakawa, M.; Hirano, M.; Kamiya, T.; Hosono, H. High electron doping to a wide band gap semiconductor $12\text{CaO}\cdot 7\text{Al}_2\text{O}_3$ thin film. *Appl. Phys. Lett.* **2007**, *90*, 182105. [[CrossRef](#)]
74. Miyakawa, M.; Ueda, N.; Kamiya, T.; Hirano, M.; Hosono, H. Novel Room Temperature Stable Electride $12\text{SrO}\cdot \text{Al}_2\text{O}_3$ Thin Films: Fabrication, Optical and Electron transport properties. *J. Ceram. Soc. Jpn.* **2007**, *115*, 567–570. [[CrossRef](#)]
75. Ebbinghaus, S.G.; Krause, H.; Lee, D.-K.; Janek, J. Single Crystals of C_{12}A_7 ($\text{Ca}_{12}\text{Al}_{14}\text{O}_{33}$) Substituted with 1 mol % Iron. *Cryst. Growth Des.* **2014**, *14*, 2240–2245. [[CrossRef](#)]
76. Sushko, P.V.; Shluger, A.L.; Hayashi, K.; Hirano, M.; Hosono, H. Photoinduced generation of electron anions in H-doped nanoporous oxide $12\text{CaO}\cdot 7\text{Al}_2\text{O}_3$: Toward an optically controlled formation of electrides. *Appl. Phys. Lett.* **2005**, *86*, 092101. [[CrossRef](#)]
77. Hayashi, K. Heavy doping of H^- ion in $12\text{CaO}\cdot 7\text{Al}_2\text{O}_3$. *J. Solid State Chem.* **2011**, *184*, 1428–1432. [[CrossRef](#)]
78. Bertoni, M.I.; Mason, T.O.; Medvedeva, J.E.; Freeman, A.J.; Poepelmeier, K.R.; Delley, B. Tunable conductivity and conduction mechanism in an ultraviolet light activated electronic conductor. *J. Appl. Phys.* **2005**, *97*, 103713. [[CrossRef](#)]
79. Dong, Y.; Hayashi, K.; Nozoe, H.; Shinoda, Y.; Hosono, H. Chloride-Ion-Stabilized Strontium Mayenite: Expansion of Versatile Material Family. *J. Am. Ceram. Soc.* **2014**, *97*, 4037–4044. [[CrossRef](#)]
80. Galuskin, E.V.; Gfeller, F.; Galuskina, I.O.; Armbruster, T.; Bailau, R.; Sharygin, V.V. Mayenite supergroup, part I: Recommended nomenclature. *Eur. J. Mineral.* **2015**, *27*, 99–111. [[CrossRef](#)]
81. Yamaguchi, O.; Narai, A.; Shimizu, K. New Compound in the System $\text{SrO}-\text{Al}_2\text{O}_3$. *J. Am. Ceram. Soc.* **1986**, *69*, C36–C37. [[CrossRef](#)]
82. Hayashi, K.; Ueda, N.; Matsuishi, S.; Hirano, M.; Kamiya, T.; Hosono, H. Solid State Syntheses of $12\text{SrO}\cdot 7\text{Al}_2\text{O}_3$ and Formation of High Density Oxygen Radical Anions, O^- and O^{2-} . *Chem. Mater.* **2008**, *20*, 5987–5996. [[CrossRef](#)]
83. Miyakawa, M.; Kobayashi, K.; Taniguchi, T. High-pressure synthesis of a $12\text{CaO}\cdot 7\text{Al}_2\text{O}_3$ — $12\text{SrO}\cdot 7\text{Al}_2\text{O}_3$ solid solution. *J. Am. Ceram. Soc.* **2017**, *100*, 1285–1289. [[CrossRef](#)]
84. Hayashi, K.; Sushko, P.V.; Hashimoto, Y.; Shluger, A.L.; Hosono, H. Hydride ions in oxide hosts hidden by hydroxide ions. *Nat. Commun.* **2014**, *5*, 3515. [[CrossRef](#)] [[PubMed](#)]
85. Miyakawa, M.; Hiramatsu, H.; Kamiya, T.; Hirano, M.; Hosono, H. Fabrication and electron transport properties of epitaxial films of electron-doped $12\text{CaO}\cdot 7\text{Al}_2\text{O}_3$ and $12\text{SrO}\cdot 7\text{Al}_2\text{O}_3$. *J. Solid State Chem.* **2010**, *183*, 385–391. [[CrossRef](#)]
86. Teusner, M.; De Souza, R.A.; Krause, H.; Ebbinghaus, S.G.; Martin, M. Oxygen transport in undoped and doped mayenite. *Solid State Ion.* **2016**, *284*, 25–27. [[CrossRef](#)]
87. Schmidt, D.A. Synthese und Charakterisierung Substituierter Mayenitphasen. Ph.D.Thesis, Technischen Universität Berlin, Berlin, Germany, 2014.
88. Maurelli, S.; Ruzsak, M.; Witkowski, S.; Pietrzyk, P.; Chiesa, M.; Sojka, Z. Spectroscopic CW-EPR and HYSCORE investigations of $\text{Cu}(2+)$ and O^{2-} species in copper doped nanoporous calcium aluminate ($12\text{CaO}\cdot 7\text{Al}_2\text{O}_3$). *Phys. Chem. Chem. Phys.* **2010**, *12*, 10933–10941. [[CrossRef](#)] [[PubMed](#)]
89. Lv, W.; Lü, W.; Guo, N.; Jia, Y.; Zhao, Q.; Jiao, M.; Shao, B.; You, H. Efficient sensitization of Mn^{2+} emission by Eu^{2+} in $\text{Ca}_{12}\text{Al}_{14}\text{O}_{33}\text{C}_{12}$ host under UV excitation. *RSC Adv.* **2013**, *3*, 16034–16039. [[CrossRef](#)]
90. Palacios, L.; Bruque, S.; Aranda, M.A.G. Structure of gallium-doped mayenite and its reduction behaviour. *Phys. Status Solidi* **2008**, *245*, 666–672. [[CrossRef](#)]
91. Irvine, J.T.S.; West, A.R. $\text{Ca}_{12}\text{Al}_{14}\text{O}_{33}$ solid electrolytes doped with zinc and phosphorus. *Solid State Ion.* **1990**, *40–41*, 896–899. [[CrossRef](#)]
92. Zhu, H.; Liu, Y.; Yan, D.; Bian, H.; Li, H.; Liu, C.; Xu, C.; Wang, X. Long lasting blue phosphorescence and photostimulated luminescence in $12\text{CaO}\cdot 7\text{Al}_2\text{O}_3:\text{Eu}$ thin films grown by pulsed laser deposition. *Opt. Mater. (Amst)* **2014**, *36*, 1771–1775. [[CrossRef](#)]
93. Zhang, J.; Zhang, Z.; Wang, T.; Hao, W. Preparation and characterization of a new long afterglow indigo phosphor $\text{Ca}_{12}\text{Al}_{14}\text{O}_{33}:\text{Nd},\text{Eu}$. *Mater. Lett.* **2003**, *57*, 4315–4318. [[CrossRef](#)]
94. Wang, R.; Zhang, Y.; Sun, J.; Liu, L.; Xu, Y. Up-conversion luminescence of Er^{3+} -doped and $\text{Yb}^{3+}/\text{Er}^{3+}$ co-doped $12\text{CaO}\cdot 7\text{Al}_2\text{O}_3$ poly-crystals. *J. Rare Earths* **2011**, *29*, 826–829. [[CrossRef](#)]
95. Liu, Y.X.; Ma, L.; Yan, D.T.; Zhu, H.C.; Liu, X.L.; Bian, H.Y.; Zhang, H.; Wang, X.J. Effects of encaged anions on the optical and EPR spectroscopies of RE doped C_{12}A_7 . *J. Lumin.* **2014**, *152*, 28–32. [[CrossRef](#)]

96. Wang, D.; Liu, Y.; Xu, C.; Liu, Y.; Wang, U.; Li, X. Local microstructure and photoluminescence of Er-doped $12\text{CaO} \cdot 7\text{Al}_2\text{O}_3$ powder. *J. Rare Earths* **2008**, *26*, 433–438. [[CrossRef](#)]
97. Liao, S.-Y.; Yao, R.; Chen, X.-Y.; Wang, G.-R.; Zheng, F. Structure refinement and up-conversion of $\text{Ho}^{3+}/\text{Er}^{3+}$ -Co-doped $12\text{CaO} \cdot 7\text{Al}_2\text{O}_3$. *Mater. Des.* **2016**, *108*, 93–105. [[CrossRef](#)]
98. Töldsepp, E.; Avarmaa, T.; Denks, V.; Feldbach, E.; Kirm, M.; Maaros, A.; Mändar, H.; Vielhauer, S. Synthesis and luminescence properties of Ce^{3+} doped nanoporous $12\text{CaO} \cdot 7\text{Al}_2\text{O}_3$ powders and ceramics. *Opt. Mater. (Amst)* **2010**, *32*, 784–788. [[CrossRef](#)]
99. Liu, X.; Liu, Y.; Yan, D.; Zhu, H.; Liu, C.; Liu, W.; Xu, C.; Liu, Y.; Zhang, H.; Wang, X. A multiphase strategy for realizing green cathodoluminescence in $12\text{CaO} \cdot 7\text{Al}_2\text{O}_3\text{-CaCeAl}_3\text{O}_7\text{:Ce}^{3+}, \text{Tb}^{3+}$ conductive phosphor. *Dalt. Trans.* **2013**, *42*, 16311–16317. [[CrossRef](#)] [[PubMed](#)]
100. Liu, X.; Liu, Y.; Yan, D.; Zhang, M.; Yang, J.; Zhu, H.; Liu, C.; Xu, C.; Wang, X. Encaged-anion tunable luminescence of Ce^{3+} -activated single host $\text{Ca}_{12}\text{Al}_{14}\text{O}_{32}\text{Cl}_2$ phosphor for UV pumped multi-color LEDs. *Mater. Des.* **2016**, *107*, 139–143. [[CrossRef](#)]
101. Zhu, H.; Liu, Y.; Yan, D.; Yan, X.; Liu, C.; Xu, C. White Luminescence of Dy^{3+} Ions Doped $12\text{CaO} \cdot 7\text{Al}_2\text{O}_3$ Nanopowders Under UV Light Excitation. *J. Nanosci. Nanotechnol.* **2011**, *11*, 9958–9963. [[CrossRef](#)] [[PubMed](#)]
102. Liu, X.; Liu, Y.; Yan, D.; Zhu, H.; Liu, C.; Xu, C.; Liu, Y.; Wang, X. Single-phased white-emitting $12\text{CaO} \cdot 7\text{Al}_2\text{O}_3\text{:Ce}^{3+}, \text{Dy}^{3+}$ phosphors with suitable electrical conductivity for field emission displays. *J. Mater. Chem.* **2012**, *22*, 16839–16843. [[CrossRef](#)]
103. Zhang, M.; Liu, Y.; Zhu, H.; Yan, D.; Yang, J.; Zhang, X.; Liu, C.; Xu, C. Enhancement of encaged electron concentration by Sr^{2+} doping and improvement of Gd^{3+} emission through controlling encaged anions in conductive C12A7 phosphors. *Phys. Chem. Chem. Phys.* **2016**, *18*, 18697–18704. [[CrossRef](#)] [[PubMed](#)]
104. Liao, S.; Yao, R.; Liu, Y.; Chen, X.; Hu, X.; Zheng, F. Green up-conversion of C12A7- Ho^{3+} prepared by co-precipitation method. *J. Alloys Compd.* **2015**, *642*, 7–14. [[CrossRef](#)]
105. Mao, Y.-Q.; Pu, Y.-P.; Wei, J.-F. Luminescence properties of Pr doped $12\text{CaO} \cdot 7\text{Al}_2\text{O}_3$ ceramics. *Mater. Res. Innov.* **2011**, *15*, 260–263. [[CrossRef](#)]
106. Zhang, X.; Liu, Y.; Zhang, M.; Yang, J.; Zhu, H.; Yan, D.; Liu, C.; Xu, C. Red-emitting nano-porous $12\text{CaO} \cdot 7\text{Al}_2\text{O}_3\text{:Sm}^{3+}$ conductive phosphor for low-voltage field emission displays. *Mater. Res. Bull.* **2017**, *86*, 51–56. [[CrossRef](#)]
107. Sato, K.; Yamaguchi, M.; Fujita, S.; Suzuki, K.; Mori, T. Enhancement of the activity of calcium aluminosilicate ($\text{Ca}_{12}\text{Al}_{10}\text{Si}_4\text{O}_{35}$) for the combustion of diesel soot via the substitution of Ca^{2+} ions with transition metal ions. *Catal. Commun.* **2006**, *7*, 132–135. [[CrossRef](#)]
108. Iimura, S.; Tomota, Y.; Matsuishi, S.; Masuda, R.; Seto, M.; Hiraka, H.; Ikeda, K.; Otomo, T.; Hosono, H. Ferrimagnetic Cage Framework in $\text{Ca}_{12}\text{Fe}_{10}\text{Si}_4\text{O}_{32}\text{Cl}_6$. *Inorg. Chem.* **2017**, *56*, 566–572. [[CrossRef](#)] [[PubMed](#)]
109. Sato, K.; Iritani, J.; Miyamoto, R.; Fujita, S.; Suzuki, K.; Ohkawa, M.; Mori, T. Reactivity of superoxide ions (O_2^-) occluded in micropores of calcium aluminosilicate varied via substitution with transition metal ions. *Stud. Surf. Sci. Catal.* **2005**, *158*, 2001–2008. [[CrossRef](#)]
110. Fujita, S.; Suzuki, K.; Mori, T. Preparation of high-performance Co_3O_4 catalyst for hydrocarbon combustion from Co-containing hydrogarnet. *Catal. Lett.* **2003**, *86*, 139–144. [[CrossRef](#)]
111. Shannon, B.Y.R.D. Revised Effective Ionic Radii and Systematic Studies of Interatomic Distances in Halides and Chalcogenides. *Acta Cryst.* **1976**, *A32*, 751–767. [[CrossRef](#)]

